Forward Modeling of Ultrasound Propagation in Layered Medium

Joyoni Dey †   Takeo Kanade ‡

joyoni.dey@cs.cmu.edu   takeo.kanade@cs.cmu.edu

CMU-RI-TR-99-02

The Robotics Institute

Carnegie Mellon University

Pittsburgh, PA 15213

June 21, 1999

† Department of ECE,

Carnegie Mellon University,

Pittsburgh PA 15213

‡ Robotics Institute,

Carnegie Mellon University,

Pittsburgh PA 15213

Chapter 1

Introduction

For many medical applications of ultrasonic devices, it is of interest to determine the distortion of ultrasound waves due to tissue inhomogeneities. Propagation of ultrasound through layered media is of interest because in various regions of the human body, the soft tissue is composed of layers of fat and muscle. Bending of the acoustic rays due to refraction at intermediate layers not only increase the lateral beam widths but also, can cause shifts in the beams (which could be as high as a few millimeters, depending on wavelength used and depth of interest), specially in cases where there is asymmetry in the intermediate layers. These effects results in degradation of resolution as well as causes geometric distortions and other artifacts in ultrasound images.

For applications such as therapeutic ultrasound, a good focussing of the ultrasonic beam is essential. It is important to evaluate the shift in the beam due to the inhomogeneities and also correct for the defocussing. Another set of applications involve ultrasound as a surgical accessory such as in computer-aided orthopedic surgeries. For example, for computer-aided Total Hip Replacement Surgery, it would be very useful if intra-operatively obtained ultrasound linear array images of bone could be used for accurate registration of pre-operative CT images of femur bone. Ultrasound is less invasive than existing registration techniques. Also, it is a cheap modality. For accurate registration however, it is necessary that the geometric distortion due to the layered inhomogeneities are estimated and compensated for.

The state of the art ultrasound scanners assume a homogeneous soft-tissue medium and an average longitudinal velocity of propagation of ultrasound at

$1540m/sec$. In reality, the velocities across different media vary considerably. Propagation velocity in typical fat layer is around $1480m/sec$ and that for muscle is around $1570m/sec$. There is also less significant within-medium variation due to temperature, compression, and various other factors such as possible directional variation due to within-medium stratification (for certain muscles).

Sound-waves propagate longitudinally in tissue; transverse or shear-waves are not transmitted very effectively through human soft-tissue [1]. However, for solid media such as bone, shear-waves are also important.

In this work, ultrasound longitudinal propagation in layered media is analytically derived, under ray-tracing approximations. Closed form expressions for the field amplitude of hemi-spherical waves has been derived for the following cases (1) transmission through a general three-layered media, (2) extension to transmission through multi-layered medium, (3) a special case of modelling the received echoes from a reflective media under two intermediate layers. This last case is of special interest for us because the scenario is akin to bone under intermediate fat-muscle layer. We are particularly interested in this case because it could be an useful tool for non-invasive tracking the skeletal bone (through fat and muscle layers) of a patient intra-operatively. A potential application is accurate intra-operative registration with pre-operative CT data.

In the derivations of the field for these cases, the interfaces between media are assumed to be arbitrary shaped, but can be broken up into small planar segments. We first derive the case for a point source emitting a spherical wave. We use ray-tracing approximations and derive the amplitude and the phase for each ray. To derive the amplitude, we apply boundary conditions to each ray at the interfaces of the media, while within each medium, the attenuation due to spreading of the wave is derived (in closed form). This spreading factor has been calculated algebraically by taking differentials of the rays and the points of intersections of the rays at the interfaces. Finally, the cross-section areas along the wavefront (locally perpendicular to the rays) are calculated.

The result can then be extended to different aperture geometries and different beam formations by delaying and summing the result for the Huygen waves emanating from each point-source forming the aperture. The analysis is extended to the broad-band pulses. Each ray "carries" a pulse with a particular amplitude and delay specific to the ray and the different pulses inter-

fere. Advantage of a closed-form equation for the field is that it is more exact than numerical evaluation. It would also simply the ray-tracing implementations in that we do not have to calculate the amplitudes by constructing an approximate ray-tube for each ray. The closed form expressions are also more amenable to non-linear inversions techniques such as Levenberg-Marquardt.

We also take into account the frequency dependent attenuation in the medium, due to absorption losses and backscattering. Losses due to viscosity has not been considered. This loss can be usually neglected.

A simulator has been built (using C) to simulate circular aperture transducers as well as linear-arrays for different media geometries. We present simulation results and compare with experiments performed on tissue mimicking phantoms for a single-element circular aperture transducer at 7.5 MHz.

1.1 Related Work in Ultrasound Propagation in Stratified Layers

Forward modelling of ultrasound propagation assuming tissues to be homogeneous stratified layers is important for some sections of the human body, such as imaging skeletal bone through layers of fat and muscle, imaging and insonification of brain-matter through the skull. There has been considerable prior work in this area [2, 3, 4, 5, 6, 7, 8].

In [6, 5, 7], ray-tracing approach is taken to evaluate the beam distortions when propagating between two media. Very interesting, experimentally validated simulation results have been presented in [6] for a 3.5 MHz, array-transducer geometrically focussed at 100 mm, showing beam displacements as high as 1.5 mm for some cases where there is asymmetry of the interface with respect to the beam axis. The theoretical approximations as detailed in [6] involve assuming that for each element of the array, the region of interest is the far-field with respect to the element-widths and the near-field with respect to the element heights. The azimuth angle of each ray is used to find the directivity-factor due to the baffle and the path-lengths of the rays in each medium are used for the range spreading.

In [3, 4], the ray-tracing approximation has been extended to refraction and reflection at multiple interfaces, considering propagation through multiple medium. Furthermore, absorption loss in the medium has been also con-

sidered. For each spherical wave, the resulting field has three-factors, first is the attenuation for the range "spreading of the wave", second the absorption loss and the third, the attenuation due to reflection of energy at previous interfaces. The last two factors have been rigorously derived. The first, range spreading factor has been determined numerically, by perturbing each ray slightly in direction and forming the ray-tube. The numerically-calculated relative cross-sectional areas of the ray-tubes gives the broadening-factor.

In [8], experiments have been done to test refraction effects on planar tissue layers, parallel to the aperture. Both fat/organ as well as skull/brain interfaces have been considered. It shows the important result that even for a symmetric interface, the skull/brain planar interface degrades resolution and introduces geometric distortion.

The exact form of the distortion that a spherical wave undergoes after refraction at an interface under ray-tracing approximations, is given in [2, 9], as described in detail in the next chapter. This analysis assumes a planar interface.

In the present work we derive a theoretical model for more general media geometries.

1.2 Applicability

The model derived here would describe the distorting effect of layered media for fairly common cases. Much of the human body is layered. We have assumed homogeneity within the individual layers. This, while somewhat restricting, is still an improvement over the state-of-the-art scanners, where the mechanism works under the assumption that the whole medium is homogeneous. Also, the within layer variations are usually not as significant as the across-medium variation. We have also assumed longitudinal propagation of sound, which is a good approximation for most soft-tissues.

The model can work as long as the ray-tracing approximation holds. For the transducer frequencies commonly used, this model is valid for near-field operations. Some calculations shown in Chapter 6 shows that the ray-tracing approximation is not very restricting. To quote a few calculations, for example, as long as we are interested in points at least $z >> 0.2017mm$ away from the interface, we can use the ray-tracing approximation for the fat-muscle interface, for a 3.5 MHz transducer. The shorter the wavelength used, the less

restricting is this criterion. For a 7.5 MHz transducer, the required depth is $z >> 0.0941mm$. The range of distances involved for the applications of interest to us are about 10 to 50 mm.

In Chapter 6 of this report we discuss some general applicability, the advantages and limitations of the model in more detail.

1.3   Contents

In the next chapter, we first give the background theory relevant to this work.

In Chapter 3, we present our derivations for three-layered media and then extend them to multi-layered media.

In Chapter 4, we present our derivations for a special case of modeling echoes received from an interface under two layers. We show that this case simply transforms in to into a case of three-layered medium.

Chapter 5, shows the experimental results on a custom-made phantoms, mimicking fat and muscle, using 7.5 MHz single element circular-aperture ultrasound transducer. We discuss results and draw conclusions.

In the last chapter we discuss the applicability of the work and mention the work in progress and future work.

Chapter 2

Background

In this chapter we give some background of ultrasound propagation and imaging.

In Section (2.1) we give the theoretical background of the different aperture integrals used to describe the field propagating into a homogeneous medium, in terms of the excited field at the aperture. The Raleigh-integral for a transducer in a rigid-baffle is of particular interest to us, in presence of absorption loss.

In Section (2.2), we give the background material for the full closed form equation of field upon reflection and refraction of a spherical wave at a single boundary [2], with and without the ray-tracing approximation. This is derived in great detail in [2] for evaluating the field propagating through two-media, separated by an interface.

2.1   Background on Ultrasonic Transducers

2.1.1   Rayleigh-Sommerfeld Equation for monochromatic waves

The wave-equation guiding the propagation of a longitudinal wave in a lossless homogeneous medium is given by [10, 11, 9, 12, 2]

$$\nabla^2 \phi = \frac{1}{C^2} \frac{\partial^2 \phi}{\partial t^2} \tag{2.1}$$

where ϕ is a scalar potential function of x, y, z, t, whose gradient is the longitudinal particle displacement, i.e, $\nabla \phi = \mathbf{u}$ where $\mathbf{u}$. C is the longitudinal-wave propagation velocity. From ϕ, all the other physical variables such as longitudinal displacement and pressure, can be deduced.

For a monochromatic wave, we get the equivalent Helmholtz equation, [10, 11, 9, 12, 2]

$$\nabla^2 \Phi(r) + k^2 \Phi(r) = 0 \tag{2.2}$$

where $k = \frac{2\pi}{\lambda}$, where $\lambda = C/f$ where f is the frequency of the wave.

This equation can be solved with different Green's functions, depending on the type of baffle the flat-piston transducer is in [10].

The two Green's functions by Sommerfeld, given in [10] (or [11]), that can be used for a rigid-baffle or a pressure-release baffle are given by

$$G = -\frac{1}{4\pi}\left(\frac{\exp(jkr_{am})}{r_{am}} \pm \frac{\exp(jk\tilde{r}_{am})}{\tilde{r}_{am}}\right) \tag{2.3}$$

where r_{am} is the distance between the apeture point and point m in the medium while $\tilde{r}_{am}$ is the distance between the aperture point and a point which is geometrically located at "mirror"-image of the point "m" with respect to the planar-aperture, illustrated in [11].

The "+ve" signed Green's function in Equation 2.3 corresponds to a transducer surrounded by a **rigid-baffle** [10]. Solving the Helmholtz equation with this function, the Rayleigh-Sommerfeld equation guiding the operation of the aperture for a particular frequency (considering a harmonic wave) for a homogeneous medium is given by

$$\Phi(P_m) = \frac{1}{2\pi} \int \int u_z(P_a) \frac{\exp(-jkr_{am})}{r_{am}} dS \tag{2.4}$$

where $k = \frac{2\pi}{\lambda}$, where $\lambda = \frac{C}{f}$ where, f is the frequency of the harmonic wave. The $u_z(P_a)$ is the aperture transmittance. This transmittance can potentially have appropriate complex weighting functions (created by lenses in optics/acoustics, or electronically in acoustics applications) creating the delays needed to focus and steer the beam emanating from the aperture. The function u_z is zero out side the transducer (i.e., on the baffle), thus the first choice of the Greens function corresponds to a rigid-baffle [10].

The physical meaning of equation 2.4 is that the response at any point in the medium, is given by the sum of all the spherical harmonic waves (Huygen's waves) emanating from the point sources composing the aperture, weighted and delayed by the appropriate transmittance of the aperture at that point.

For the second choice of the Green's function (with "-ve" sign) in Equation 2.3, we would get what is appropriate for a **pressure-release baffle**, for which the pressure is zero on the baffle [10]. Using this, the aperture equation is,

$$\Phi(P_m) = \frac{jk}{2\pi} \int \int \Phi(P_a) \frac{\exp(-jkr_{am})(1 + 1/jkr_{am})}{r_{am}} \cos(\hat{n}, \hat{r_{am}}) dS \quad (2.5)$$

This, for regions where the radius $r_{am} >> \lambda$, we can ignore kr_{am} with respect to 1 and get,

$$\Phi(P_m) = \frac{jk}{2\pi} \int \int \Phi(P_a) \frac{\exp(-jkr_{am})}{r_{am}} \cos(\hat{n}, \hat{r_{am}}) dS \quad (2.6)$$

This equation has the added cosine factor, called the directivity function or the obliquity function.

2.1.2 Rayleigh-Sommerfeld Equations for an emitted Pulse

In many cases, the incident field is not a monochromatic wave, but a pulse, with a range of frequencies. The generalization of the Rayleigh-Sommerfeld theory to these non-monochromatic waves is given in Section 3-5 in [11].

For a **rigid baffle**, the phase in the Equation 2.4 gives the time delays of the pulses, resulting in the so-called *Raleigh integral*,

$$\phi(P_m, t) = -\frac{1}{2\pi} \int \int \frac{1}{r_{am}} u_z(P_a, t - \frac{r_{am}}{C}) dS \quad (2.7)$$

But the $\frac{1}{\lambda} = \frac{f}{C}$ term in the Equation 2.6 results in another interesting effect that disturbance in the medium is the time derivative of the disturbance in the aperture (apart from the delay).

Thus for a **pressure-release baffle** the disturbance in the medium is given by,

8

$$\phi(P_m, t) = \int \int \frac{\frac{d}{dt}\phi(P_a, t - \frac{r_{am}}{c})}{2\pi C r_{am}} \cos(\hat{n}, \hat{r_{am}}) dS \qquad (2.8)$$

2.1.3 Rigid-Baffle vs. Pressure-Release Baffle

Examples of rigid-baffle and pressure-release baffle are given in [10], at the end of Section 3.2.1 (Pg. 171). For example, a transducer in water, surrounded by a metal disk whose impedance is much higher than that of water, would be one in a rigid-baffle. A transducer in a pressure-release baffle would be a small transducer (dimensions of one wavelength or less) or one element of an array of identical transducers, separated by a distance of a wavelength or more, separated from a water-bath, by a Mylar film, such that there is air on one side of the film and water on the other side.

An ultrasound array has an angular response somewhere in between that of a source in a rigid-baffle and that in a pressure-release baffle [3]. In this work, as in most simulations, we have assumed the Raleigh Integral (that is the equation for a rigid-baffle) given in Equation 2.7. This gives good results near the axis.

For more details on baffled planar pistons, the excellent paper [13] or [14] are referred.

2.1.4 Linear-Arrays : focussing and steering

Different aperture transmittance functions can be applied to focus and steer the beam emanating from an aperture. The concepts are similar to focussing lens in optics [11]. For acoustical applications, since sound velocities are much lower than the electronic delaying speeds, the aperture can be broken up into little elements and each element can be delay-triggered according to what sort of beam is needed. The mathematical details can be found in many books and papers, such as [11, 10, 15, 16, 17], to cite a few.

Here we briefly give the intuitive idea behind the focussing. To focus at a point $z = r_f$, a curve given by $u_z(P_a) = \exp(-jkr_f)$ is required across the aperture. That is, instead the triggering all of the elements of the array at once, they are triggered with delays such that, for a uniform known velocity of the medium, the waves from all the elements would reach the point of focus in phase at the same instant. The delays would exactly compensate

9

for the path-differences. Figure 2.1 shows focussing the aperture (composed of small rectangular elements) when transmitting.
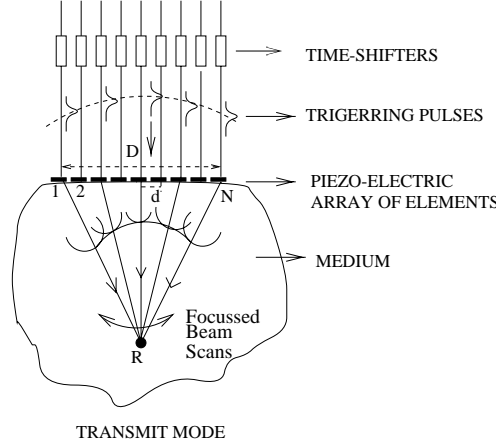

Figure 2.1: **Transmit Focus**

There could be focussing during receiving as well, shown in Figure 2.2. The wave reaching "R" is scattered or reflected back. The signal coming back reaches the element just above it first, and the other elements later, delayed by the path-differences. Hence the signals received are delayed (by the same curve as on transmit-focus) according to the path-differences again and added in phase.

The focussed beam can be steered to right/left as well, if we add a "linear" delay across the aperture in addition to the focussing-delays (which are almost "quadratic"-delays for focussing distance large compared to the aperture dimensions). Refer to Figure 2.3.

2.1.5 Disturbance in a homogeneous non-viscous medium with absorption loss

To consider absorption loss, the state equation used to derive the wave-equation can be modified as shown in [3] to incorporate absorption loss. The effect is that the k in the Helmholtz Equation 2.2 is complex as shown in [3, 2]. The complex k results in a factor $e^{-\mu r_{am}}$ multiplied to the *intensities*. Here μ is given by $\mu = RK\frac{\omega^2}{c}$, where K is the compressibility and R (which maybe a
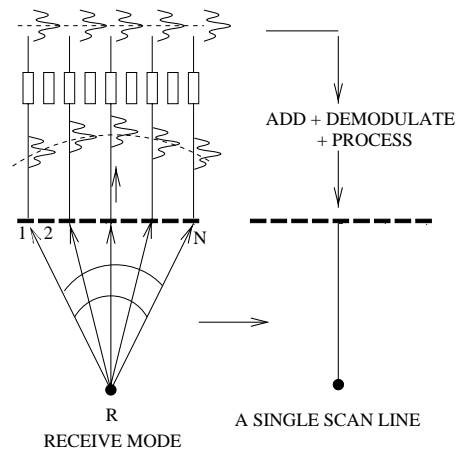
10

ADD + DEMODULATE
+ PROCESS

1 2   N

R
RECEIVE MODE

A SINGLE SCAN LINE

Figure 2.2: **"Listen" in Focus**

F_0 F_n
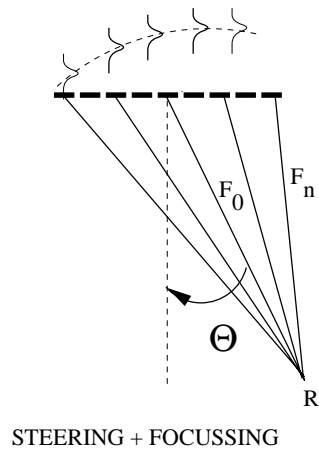
Θ

R

STEERING + FOCUSSING

Figure 2.3: **Steering and Focussing**

11

function of frequency) is the proportionality factor relating the rate of change of the normalized mass-density, to the energy absorbed (and transformed to heat) [3].

For multiple layers, under ray-tracing approximation, the absorption loss results in the intensities getting multiplied by a series of exponentials, i.e, $e^{-(\mu_1 L_1 + \mu_2 L_2 + ...)}$, where $L_1, L_2...$ are the distances travelled by the ray in successive media.

Note : The other two equations that are used to derive the wave-equation are the conservation of mass and momentum. For fluids with viscous loss, the momentum conservation equation has to be modified. This effect is not considered in this work.

2.2 Reflection and Refraction of A Spherical Wave with one layer of inhomogeneity

Since the aperture Equations 2.4 and 2.6 are basically summing up the responses of the spherical waves emanating from each point in the aperture, it is of interest to see what happens to a spherical wave upon reflection and refraction at a planar boundary, referring to Figures 2.4 and Figure 2.5.
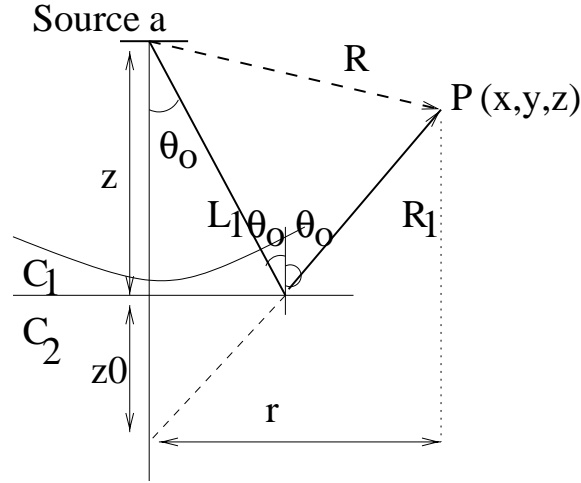

Figure 2.4: **Reflection a of Spherical Wave**

Figure 2.5: **Refraction of Spherical Wave**

2.2.1 Exact Waveforms

The exact waveforms after refraction and reflection for a single intermediate layer is derived in [2]. The approach was to break up the spherical wave into a series of plane waves Equations 26.17 (or 26.19) in [2] and apply the boundary conditions for reflection and refraction for each of these plane waves.

The **reflected waveform** is found in [2], Equation 26.27, as

$$G_{refl}(P) = (ik/2) \int_{-\pi/2+i\infty}^{\pi/2-i\infty} H_0^{(1)}(u) e^{ik(z+z_0)\cos\theta} V(\theta) \sin\theta d\theta \qquad (2.9)$$

where, $H_0^{(1)}(u)$ is the Hankel function of first kind, and the argument $u = kr\sin\theta$.

The total waveform at a point P in the first media is the sum of the wave directly incident on P and the reflected wave,

$$G_{total}(P) = \frac{e^{ikR}}{R} + G_{refl}(P) \qquad (2.10)$$

The **refracted waveform** is found in [2], Page 280, as

$$G_{refr}(P) = \frac{ik}{2\pi m} \int_0^{\pi/2-i\infty} \int_0^{2\pi} \exp[i(k(x\cos\phi + y\sin\phi)\sin\theta$$

13

$$+kz_0 \cos\theta + k_1 z \cos\theta_1)](1 + V(\theta)) \sin\theta d\theta d\phi \qquad (2.11)$$

2.2.2   Ray-Tracing approximation and correction terms

Different approximations of the exact equations can be obtained as derived in Section 27-28 and Section 32 of the book [2].

When we $1/(kR_1)^2 << 1$, the approximate **reflected wave** is (from Equation 28.13 in [2]).

$$G_{refl}(P) = \frac{e^{jk_1R_1}}{R_1}[V(\theta_0) - jN/kR_1] \qquad (2.12)$$

where

$$N = \frac{1}{2}[V''(\theta_0) + V'(\theta_0)\cot\theta_0] \qquad (2.13)$$

where $V'(\theta_0)$ and $V''(\theta_0)$ are first and second derivatives with respect to θ (evaluated at θ_0).

The first term, $G_{refl}(P) = \frac{e^{jk_1R_1}}{R_1}V(\theta_0)$ gives the **geometric-optics** or **ray-tracing approximation**. This approximation indicates the reflection coefficient of the spherical wave is the same as that of the component plane waves. The physical structure of the reflected wave under ray-tracing approximation is spherical, as can be seen from the equation, as well as deduced from the geometry. The other physical interpretation is that this approximation means that the field at the observation point P in Figure 2.4 is composed of mainly the component plane waves close to $\theta = \theta_0$.

The "correction term" is important only if the source and the receiver are close to the boundary, compared to the wavelength [2].

The **refracted wave** with geometric-optics approximation and the first correction term are given for $n > 1$ and $n < 1$ in Equations 32.11 and 32.12 in [2], not reproduced here.

The criterion under which the "correction" term can be neglected are given as follows.

Referring to Figure 2.5, for $n > 1$, geometric-optics criterion would be valid if the elevation of the source is high enough from the boundary compared to the wavelength. The observation point position is not that important.

$$k_1 z_0 >> \frac{m}{\sqrt{n^2 - 1}} \qquad (2.14)$$

where $m = \rho_2/\rho_1$ and $n = C_1/C_2$ (where ρ denotes the density and C denotes velocity, n is the relative refractive index).

However, for $n < 1$, the observation point needs to be far from the boundary, while the position of the source is not that important.

$$k_1 z >> \frac{1}{\sqrt{1 - n^2}} \qquad (2.15)$$

The equation for geometric optics approximation for a spherical wave after refraction at a planar interface is derived in Eqn. 32.8, page 279 of [2] (as well as in [9], page 411). This is derived from a geometric viewpoint by taking a ray and perturbing it by $d\theta$ as shown in Figure 2.5. The proof is not reproduced here, but the main idea behind the derivation of the *amplitude* is that at the boundary, one applies the boundary conditions (continuity of the total wave above and below) to get the relationship between the waves just above and just below T. In the second medium, there is attenuation due to "spreading of the wave" is given by the conservation of energy in annular-regions swept by Area A_1 and A_2, that is, the amplitude "drop" between point T in the medium and the point m is given by $\sqrt{\frac{2\pi r_2 A_2}{2\pi r_1 A_1}}$. These concepts are adopted in the next section where we derive the closed form amplitude for the more general cases. The *phase* is given simply as the $\exp(jk_1 L_1 + jk_2 L_2) = \exp[jk_1(L_1 + nL_2)]$, that is the delays in the time domain are simply the path-lengths in the two media divided by their corresponding velocities. The resulting waveform is given by,

$$G(P_m) = A(P_a, \theta, n) \exp(jk_1 L_1 + jk_2 L_2) \qquad (2.16)$$

The amplitude is given by

$$A(P_a, \theta, n) = \frac{\sqrt{\sin\theta} \exp[jk_1(L_1 + nL_2)]}{(m\cos\theta + n\cos\theta_1)\sqrt{[L_1 \sin\theta + (L_2)\sin\theta_1][L_1 \cos^{-2}\theta + \frac{L_2}{n}\cos^{-2}\theta_1]}} \qquad (2.17)$$

15

2.2.3 Aperture Equation With Ray-Tracing Approximation

We attempt to obtain the aperture equation by modifying the Raleigh integral using the above $G(P_m)$, (in Equation 2.16).

$$\Phi(P_m) = \int_{P_a} \int A(P_a, \theta, n) u_z(P_a) \exp(jk_1 L_1 + jk_2 L_2) dS \qquad (2.18)$$

For $n = 1$, the amplitude is $A(P_a, \theta, n) = \frac{1}{r_{am}}$, (as expected for a spherical wave) and Equation 2.18 reduces to the equation for the aperture in a rigid-baffle.

In the next chapter we derive the received field amplitude and phase for more general cases.

16

Chapter 3

Ray-Tracing of Ultrasound Field Propagation through Layered Medium

In this chapter we derive the function modeling the ultrasound field propagating through layered media under ray-tracing approximations. In the next two sections, we present a closed form equation for the field for (1) propagation through 3-layered media and extend it to (2) multiple media. A third section deals with (3) a special case of imaging a reflective media under two layers, which we reduce to the problem of propagation through three media.

3.1 Propagation in a three-layered medium

In this section we derive the propagation equations through three layers and then generalize to multiple layers. The assumptions are that each of the layers are homogeneous within themselves. The other assumption is that ray-acoustics approximation is valid for the relative dimensions of the layers considered and the wavelength used. The third assumption is that interfaces separating the media are locally planar (to the order of the wavelength used).

In Figure 3.1 we illustrate the rays propagating through three media. First we show an aperture which is idealized to be composed of point sources, emitting hemispherical waves into the first medium in contact. Then we trace a ray passing through Medium 1, 2, 3, with acoustic propagation velocities
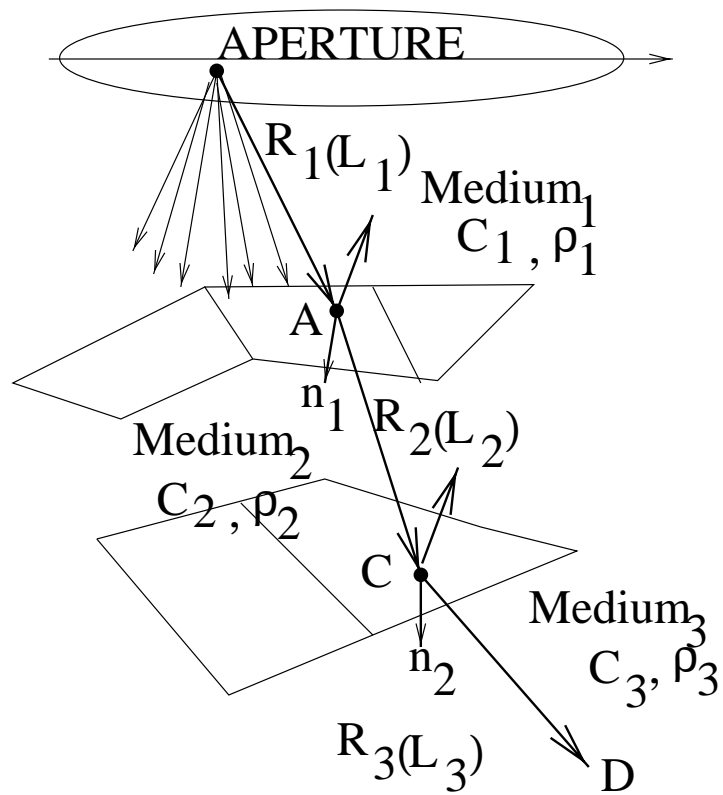
Figure 3.1: **Ultrasound Rays Through Three Layers**

C_1, C_2 and C_3 and densities ρ_1, ρ_2 and ρ_3 respectively. The ray is partly reflected and partly transmitted at every interface. In this derivation, we do not consider absorption, however it can be incorporated by using the factors mentioned in Section 2.1.5. In Figure 3.1 the different sections of rays in the different media are denoted by vectors $\mathbf{R_1}$, $\mathbf{R_2}$, ... etc. The corresponding lengths of the rays are (denoted in brackets), L_1, L_2, ... etc.

Conceptually, we follow the approach taken in [2, 9] to analyze the refraction of a spherical wave at a single planar surface. At the boundary of successive layers, we apply boundary conditions (continuity of pressure) to obtain the relationship between the field just below and just above the interface. Within the media we take into account the attenuation due to "spreading of the wave".
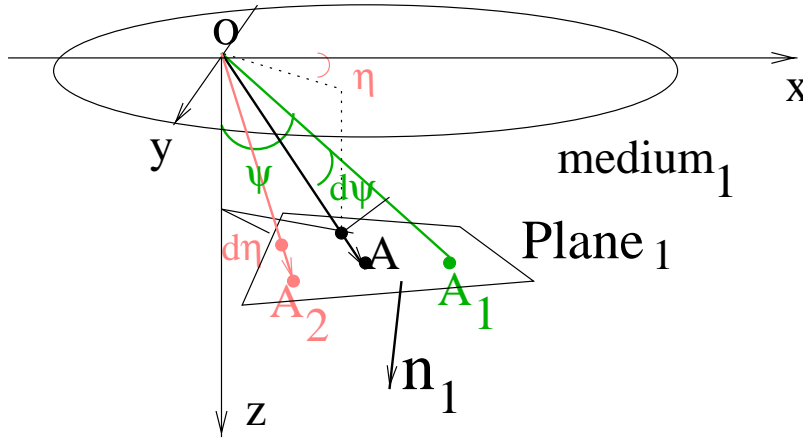

Figure 3.2: **Considering Differential Rays in Two Directions**

To calculate the spreading factor which we term as SF henceforward, we compose a differential "flux-tube" composed of three rays - the ray in consideration and two other rays obtained by shifting differentially from this ray, as shown in Figure 3.2. In absence of absorption or viscosity loss, energy is conserved across flux tube areas perpendicular to the ray. The area, perpendicular to the ray locally signifies the wavefront. The attenuation factor due to spreading, is given by the square-root of the inverse ratio of the flux-tube cross-sectional areas [2, 9]. In our derivations the areas are of differential dimensions. However they are all derived to a common differential measures, which get cancelled when we calculate their ratios. As shown, the attenu-

19

ation factors can be obtained as functions of the various ray's lengths and directions and the directions perpendicular to the rays and the normals to the planes.

The co-ordinate system we consider is shown in Figure 3.2. The plane of the aperture is the x-y plane and z-axis is downward into the media. The origin is shifted to the source point we consider. We define the ray in spherical-coordinates. ψ is the angle the ray makes with the z-axis and η is the angle the projection makes with the x-axis. The flux-tube we construct is illustrated in Figure 3.2. To form the flux-tube, another ray is by perturbing the ray slightly to another angle $\psi+\mathrm{d}\psi$ (keeping η fixed). The origin is the same. We call this the $\mathrm{d}\psi$-ray henceforward. Similarly, another is ray is obtained by perturbing the ray by an angle $\mathrm{d}\eta$ (keeping ψ fixed). We call this the $\mathrm{d}\eta$-ray henceforward. The primary ray, is called the main-ray from now on.

The ray, the ψ-ray and the η-ray hit the first planar segment (interface between the first and the second medium) at points A, A_1 and A_2 respectively.

Figure 3.3 shows (from another viewpoint) the three-rays undergoing refraction at the two interfaces. The shaded triangles AA_1A_2 and CC_1C_2 are the vertices of intersection of the rays with the (locally planar) interfaces. However the areas *perpendicular* to the ray are the unshaded ones. The areas of these are the ones to be considered for calculation of attenuation.

We refer to Figures 3.1 and 3.3 in our derivations. We intend to derive the field at the point D given that a spherical wave emitted, from an *unit-powered* source O, is incident at the point A (Figure 3.1).

The phase-shift between the emitted field at O and and the field at D is obtained straightforwardly as a function of the time-delay in each media. The phase is given simply as,

$$\Phi = \exp[j(2\pi f)(\frac{L_1}{C_1} + \frac{L_2}{C_2} + \frac{L_3}{C_3})] \tag{3.1}$$

Henceforward we consider the derivation of the amplitude at D.

The field just above A is the sum of the incident (spherical) wave and the reflected wave. Hence,

$$|f_A|_{above} = \frac{|1 + V(\theta)|}{L_1} \tag{3.2}$$
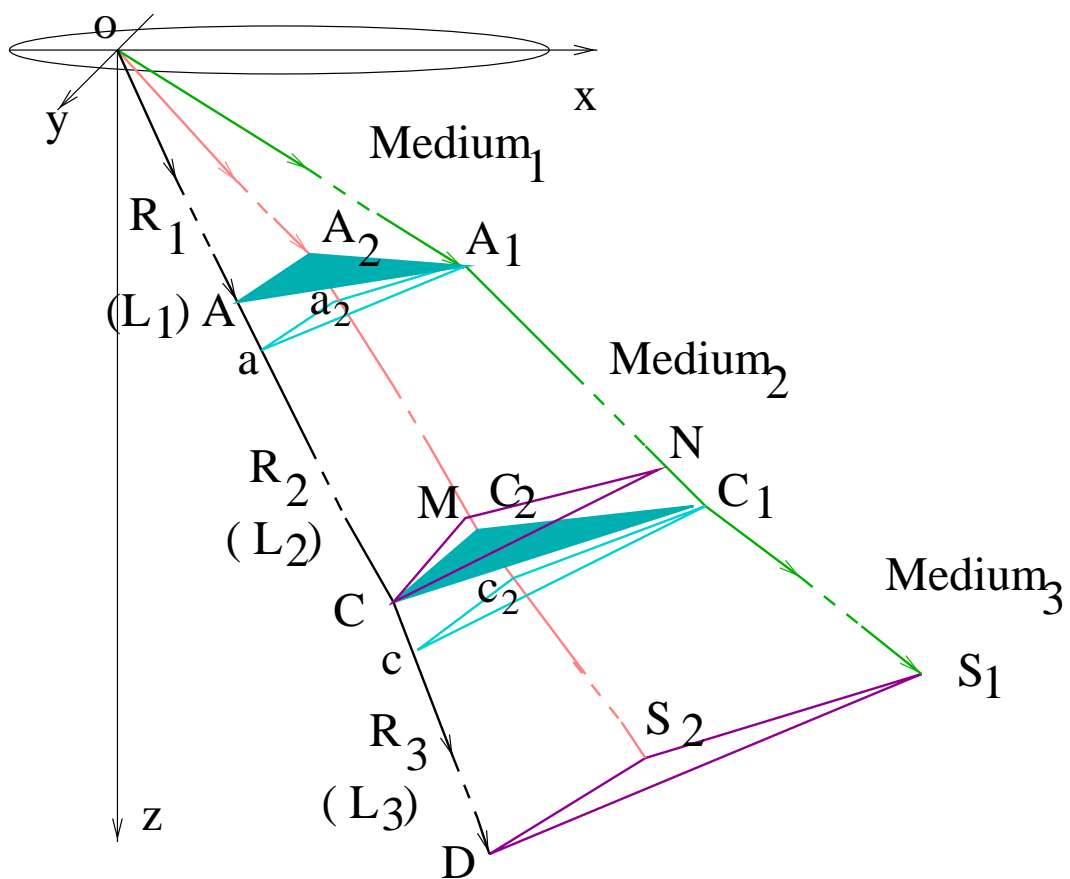
where $V(\theta)$ is the reflection coefficient given by

Figure 3.3: **Areas of Energy Conservation**

$$V(\theta) = \frac{m\cos\theta - \sqrt{n^2 - \sin^2\theta}}{m\cos\theta + \sqrt{n^2 - \sin^2\theta}} \qquad (3.3)$$

where θ is the angle of incidence at the first interface (that is, angle between $\mathbf{R_1}$ and normal $\mathbf{n_1}$), $m = \frac{\rho_2}{\rho_1}$ (that is the density ratio of second-medium to the first), $n = \frac{C_1}{C_2}$ is the refractive index of the first-medium to that in the second-medium.

At the boundary, we use the continuity of pressure condition, which in turn gives, the relation for the field potential as [2], $\rho_1 f_1 = \rho_2 f_2$, where ρ is the density, and f_1 and f_2 are the field potentials in the two media respectively, above and below the point in question.

Hence, just below A, by boundary conditions of continuity of pressure, the field is just $\frac{1}{m}$ times the field above A.

$$|f_A|_{below} = \frac{|1 + V(\theta)|}{mL_1} \qquad (3.4)$$

In Medium 2, to obtain the field at C we have to consider the attenuation factor between A and C. To obtain this, we refer to Figure 3.3. The plane perpendicular to the second section of the ray R_2 Δaa_2A_1 is obtained where the plane perpendicular to the main ray $\mathbf{R_2}$ (in the second medium) intersects the dψ-ray (at A_1) and the dη-ray (at a_2). The triangle, Δaa_2A_1 is a projection of ΔAA_1A_2 on to the plane perpendicular to $\mathbf{R_2}$ at A, ignoring lengths of second order of differentials (that is of form dldl) compared to length of a single order (dl) [1]. Δaa_2A_1 is, therefore the flux tube crossectional-area just under A.

At point C, the cross-sectional area of the flux tube is given by $Area\Delta CMN$ (area perpendicular to $\mathbf{R_2}$ at C).

The spreading attenuation is given by,

---

[1]Note that the projection would have been exact if the vector $\mathbf{A_2a_2}$ had been parallel to $\mathbf{Aa}$. But the difference is negligible. Let us consider a point $a_2{}'$ on the plane perpendicular to $\mathbf{R_2}$, such that $\mathbf{A_2a_2{}'}$ is parallel to $\mathbf{Aa}$. This would be the exact projection of A_2 on to this plane. The difference between $a_2{}'$ and a_2 is given by arc swept by A_2a_2 in going through a differential angle (the angular difference between the $\mathbf{R_2}$ and its dη-ray counterpart). Since A_2a_2 is by itself of differential length, the arc is therefore of second order differential, of negligible dimensions. That is a_2 and $a_2{}'$ are virtually coincident in this differential world.

$$SF_2 = \sqrt{\frac{Area \Delta aa_2 A_1}{Area \Delta CMN}} \tag{3.5}$$

The suffix 2 on SF denotes that this is in Medium 2. We come back later to deriving these factors in terms of the rays and the parameters of the medium.

Hence, we get at C, just before the boundary, the field is,

$$|f_C|_{inc} = |f_A|_{below} SF_2 \tag{3.6}$$

where the suffix inc indicates the incident field just above C.

We proceed similarly along the ray to find the field just below C and then consider the attenuation to obtain field at D.

Applying boundary conditions at C, and get,

$$\begin{aligned} |f_C|_{below} &= |f_C|_{inc} \frac{1 + V'(\theta_t)}{m'} \\ &= \frac{|1 + V(\theta)|}{mL_1} \frac{1 + V'(\theta_t)}{m'} SF_2 \end{aligned} \tag{3.7}$$

where, $m' = \frac{\rho_3}{\rho_2}$ and

$$V'(\theta_t) = \frac{m' \cos \theta_t - \sqrt{n'^2 - \sin^2 \theta_t}}{m' \cos \theta_t + \sqrt{n'^2 - \sin^2 \theta_t}} \tag{3.8}$$

Here θ_t is the angle of incidence at second interface (that is, angle between $\mathbf{R_2}$ and normal $\mathbf{n_2}$) and $n' = \frac{C_2}{C_3}$ is the relative refractive index between Medium 2 and Medium 3.

Finally going from C to D, we have to consider the attenuation factor SF_3, given by,

$$SF_3 = \sqrt{\frac{Area \Delta cc_2 C_1}{Area \Delta DS_2 S}} \tag{3.9}$$

The amplitude of the field at D, is therefore,

$$|f_D| = \frac{|1 + V(\theta)|}{mL_1} \frac{|1 + V'(\theta_t)|}{m'} (SF_2)(SF_3) \tag{3.10}$$
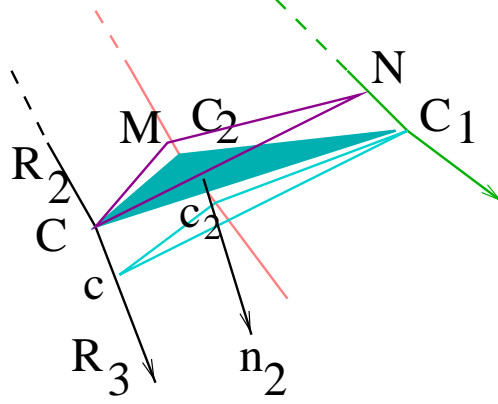
23

Figure 3.4: **Projections of Area**

But the product of the spreading factors in the different media $(SF_2)(SF_3)$ can be simplified if we refer to Figure 3.4. This shows the two cross-sectional triangles just above and just below the point C.

$Area\Delta CMN$ is the projection of $Area\Delta CC_2C_1$ onto a plane perpendicular to ray $\mathbf{R_2}$ and $Area\Delta cc_2C_1$ is the projection of $Area\Delta CC_2C_1$ onto a plane perpendicular to ray $\mathbf{R_3}$. Hence, by laws of orthogonal projection, $Area\Delta CMN = \cos\theta_t Area\Delta CC_2C_1$ and $Area\Delta cc_2C_1 = \cos\theta_t' Area\Delta CC_2C_1$, where θ_t is the angle of incidence (angle between $\mathbf{n_2}$ and $\mathbf{R_2}$) and θ_t' is the angle of refraction at the interface (angle between $\mathbf{n_2}$ and $\mathbf{R_3}$).

Hence, we can write

$$
\begin{aligned}
(SF_2)(SF_3) &= \sqrt{\frac{Area\Delta aa_2A_1}{Area\Delta CMN}}\sqrt{\frac{Area\Delta cc_2C_1}{Area\Delta DS_2S_1}} \\
&= \sqrt{\frac{Area\Delta aa_2A_1}{Area\Delta DS_2S_1}}\sqrt{\frac{\cos\theta_t'}{\cos\theta_t}} \qquad (3.11)
\end{aligned}
$$

We have to therefore derive only the last (ΔDS_2S_1) and the first (Δaa_2A_1) areas.

The closed form derivation of the area ratios is the most elaborate portion of the derivation as well as the major original contribution of this work. In this chapter, we mention the main idea behind the derivations and present the final results we arrived at. We leave the details to Appendix A.

To derive the areas, we derive the sides of the triangles first. To briefly outline the proof, we derive the equations of the rays and find the points of intersections of rays and the planes. Then we differentiate the equations for the points of intersections to arrive at the sides of the triangles formed by the points of intersections (shaded triangles in Figure 3.3). From these we can arrive at the unshaded triangles progressively.

We consider the vectors $\mathbf{aA_1}$ and $\mathbf{aa_2}$ of the triangle Δaa_2A_1 first. Referring to the Figure 3.3, these are obtained from first deriving the sides of another triangle ΔAA_2A_1. The main ray and its differentially perturbed rays in two directions intersects the first planar segment forming triangle ΔAA_2A_1. We can then derive the sides of the triangle Δaa_2A_1 from those of ΔAA_2A_1.

The vector $\mathbf{aA_1}$ is derived in Appendix A as

$$
\begin{aligned}
\mathbf{aA_1} \quad = \quad & L_1 d\psi [\hat{\mathbf{x}}_{1\psi} - \frac{(\mathbf{n_1} \cdot \hat{\mathbf{x}}_{1\psi})}{(\mathbf{n_1} \cdot \hat{\mathbf{R}}_1)} \hat{\mathbf{R}}_1 \\
& - ((\hat{\mathbf{x}}_{1\psi} \cdot \hat{\mathbf{R}}_2) - \frac{(\mathbf{n_1} \cdot \hat{\mathbf{x}}_{1\psi})(\hat{\mathbf{R}}_1 \cdot \hat{\mathbf{R}}_2)}{(\mathbf{n_1} \cdot \hat{\mathbf{R}}_1)}) \hat{\mathbf{R}}_2] \quad (3.12)
\end{aligned}
$$

where $\hat{\mathbf{R}}_1$ and $\hat{\mathbf{R}}_2$ are the ray-vectors, $\hat{\mathbf{x}}_{1\psi}$ is given in Equation A.6. $\mathbf{n_1}$ is the normal to the first interface, and the length L_1 is the intercept of ray $\hat{\mathbf{R}}_1$ at the first medium.

The second vector side of triangle Δaa_2A_1, is $\mathbf{aa_2}$. This is (neglecting second order differences) derived as

$$
\begin{aligned}
\mathbf{aa_2} \quad = \quad & L_1 d\eta [\hat{\mathbf{x}}_{1\eta} - \frac{(\mathbf{n_1} \cdot \hat{\mathbf{x}}_{1\eta})}{(\mathbf{n_1} \cdot \hat{\mathbf{R}}_1)} \hat{\mathbf{R}}_1 \\
& - ((\hat{\mathbf{x}}_{1\eta} \cdot \hat{\mathbf{R}}_2) - \frac{(\mathbf{n_1} \cdot \hat{\mathbf{x}}_{1\eta})(\hat{\mathbf{R}}_1 \cdot \hat{\mathbf{R}}_2)}{(\mathbf{n_1} \cdot \hat{\mathbf{R}}_1)}) \hat{\mathbf{R}}_2] \quad (3.13)
\end{aligned}
$$

where

vector $\hat{\mathbf{x}}_{1\eta}$ is the direction of the derivative of the $\hat{\mathbf{R}}_1$ (with respect to η) as shown in Equation A.41.

Using these relations for the sides, the area Δaa_2A_1 can be obtained as,

$$
Area\Delta aa_2A_1 = |\mathbf{aA_1} \times \mathbf{aa_2}| \qquad (3.14)
$$

Note there is factor L_1^2 in this cross-product. Under the square root, of Equation 3.11, this would result in a factor of L_1 to get cancelled with the $1/L_1$ in Equation 3.9. The measure $d\psi d\eta$ in this cross-product gets cancelled with the same ratio in the area in the denominator of Equation 3.11. This second area, that of $\Delta DS_2 S_1$ is of interest next.

The sides of this triangle can be derived from sides of the triangle $\Delta CC_2 C_1$ and the additional "arcs" swept by the length L_3, in bending from $\hat{\mathbf{R}}_3$ to the differential lengths in each direction, as shown in Figure A.2.

The expression for $\mathbf{DS_1}$ can be obtained by substituting Equations A.34 and A.30 in Equation A.32, as repeated below.

$$\mathbf{DS_1} = \delta_\psi \mathbf{P_C} - (\hat{\mathbf{R}}_3 \cdot \delta_\psi \mathbf{P_C})\hat{\mathbf{R}}_3 + L_3(\delta_\psi \hat{\mathbf{R}}_3) \qquad (3.15)$$

where $\delta_\psi \mathbf{P_C}$ and $\delta_\psi \hat{\mathbf{R}}_3$ are given as

$$
\begin{aligned}
\delta_\psi \mathbf{P_C} =\ & (d\psi)[L_1(\hat{\mathbf{x}}_{1\psi} - \frac{(\mathbf{n_1} \cdot \hat{\mathbf{x}}_{1\psi})}{(\mathbf{n_1} \cdot \hat{\mathbf{R}}_1)}\hat{\mathbf{R}}_1) \\
& - L_1 \hat{\mathbf{R}}_2 \left(\frac{(\mathbf{n_2} \cdot \hat{\mathbf{x}}_{1\psi})(\mathbf{n_1} \cdot \hat{\mathbf{R}}_1) - (\mathbf{n_1} \cdot \hat{\mathbf{x}}_{1\psi})(\mathbf{n_2} \cdot \hat{\mathbf{R}}_1))}{(\mathbf{n_1} \cdot \hat{\mathbf{R}}_1)(\mathbf{n_2} \cdot \hat{\mathbf{R}}_2)} \right) \\
& + L_2 \hat{\mathbf{x}}_{2\psi} - L_2 \hat{\mathbf{R}}_2 \frac{(\mathbf{n_2} \cdot \hat{\mathbf{x}}_{2\psi})}{(\mathbf{n_2} \cdot \hat{\mathbf{R}}_2)}]
\end{aligned}
\qquad (3.16)
$$

and

$$\delta_\psi \hat{\mathbf{R}}_3 = \frac{d\psi}{n'}[\hat{\mathbf{x}}_{2\psi} - \mathbf{n_2}(1 - \frac{\tan \theta_t'}{\tan \theta_t})(\mathbf{n_2} \cdot \hat{\mathbf{x}}_{2\psi})] \qquad (3.17)$$

where $\hat{\mathbf{x}}_{1\psi}$ and $\hat{\mathbf{x}}_{2\psi}$ are given in Equations A.6, A.26 respectively.

Similarly, $\mathbf{DS_2}$ is given by

$$\mathbf{DS_2} = \delta_\eta \mathbf{P_C} - (\hat{\mathbf{R}}_3 \cdot \delta_\eta \mathbf{P_C})\hat{\mathbf{R}}_3 + L_3(\delta_\eta \hat{\mathbf{R}}_3) \qquad (3.18)$$

where $\delta_\eta \mathbf{P_C}$ and $\delta_\eta \hat{\mathbf{R}}_3$ are given by

$$\delta_\eta \mathbf{P_C} \quad = \quad (d\eta)[L_1(\hat{\mathbf{x}}_{1\eta} - \frac{(\mathbf{n_1} \cdot \hat{\mathbf{x}}_{1\eta})}{(\mathbf{n_1} \cdot \hat{\mathbf{R}}_1)}\hat{\mathbf{R}}_1)$$

$$-L_1\hat{\mathbf{R}}_2(\frac{(\mathbf{n_2} \cdot \hat{\mathbf{x}}_{1\eta})(\mathbf{n_1} \cdot \hat{\mathbf{R}}_1) - (\mathbf{n_1} \cdot \hat{\mathbf{x}}_{1\eta})(\mathbf{n_2} \cdot \hat{\mathbf{R}}_1))}{(\mathbf{n_1} \cdot \hat{\mathbf{R}}_1)(\mathbf{n_2} \cdot \hat{\mathbf{R}}_2)})$$

$$+L_2\hat{\mathbf{x}}_{2\eta} - L_2\hat{\mathbf{R}}_2\frac{(\mathbf{n_2} \cdot \hat{\mathbf{x}}_{2\eta})}{(\mathbf{n_2} \cdot \hat{\mathbf{R}}_2)}] \qquad (3.19)$$

and,

$$\delta_\eta \hat{\mathbf{R}}_3 \quad = \quad \frac{d\eta}{n'}[\hat{\mathbf{x}}_{2\eta} - \mathbf{n_2}(1 - \frac{\tan\theta_t^{'}}{\tan\theta_t})(\mathbf{n_2} \cdot \hat{\mathbf{x}}_{2\eta})] \qquad (3.20)$$

where $\hat{\mathbf{x}}_{1\eta}$, $\hat{\mathbf{x}}_{2\eta}$ are given in Equations A.41, A.46 respectively.

So, we are ready to arrive at the area of triangle ΔDS_2S_1 by using the lengths $\mathbf{DS_1}$ and $\mathbf{DS_2}$ to get,

$$Area\Delta DS_2S_1 = |\mathbf{DS_1} \times \mathbf{DS_2}| \qquad (3.21)$$

Note that this area has the measure differential measure $d\psi d\eta$ which gets cancelled with the same measure in Equation 3.14 when we take the ratio of the two, in Equation 3.11.

3.2 Propagation in multi-layered medium

We extend the analysis in the last section to the case where there are multiple layers in the media.

Again the time-delays encountered in each medium constitute the phase factor. Inside the i-th medium, at the point $\mathbf{D_i}$, the phase is given by,

$$\Phi_i = \exp[j(2\pi f)(\frac{L_1}{C_1} + \frac{L_2}{C_2} + ... + \frac{L_i}{C_i})] \qquad (3.22)$$

To obtain the amplitude at the point $\mathbf{D_i}$ at the i-th layer, Equation 3.10 can be extended to

$$|f_{D_i}| = \frac{|1 + V_{12}(\theta_{12})|}{m_{12}L_1} \frac{|1 + V_{23}(\theta_{23})|}{m_{23}} ... \frac{|1 + V_{(i-1)i}(\theta_{(i-1)i})|}{m_{(i-1)i}}(SF_2)(SF_3)...(SF_i)$$

$$(3.23)$$

The spreading factor $(SF_2)(SF_3)...(SF_i)$ can be similarly derived as square root of the area of the first and the last triangles with the chain of cosine factors.
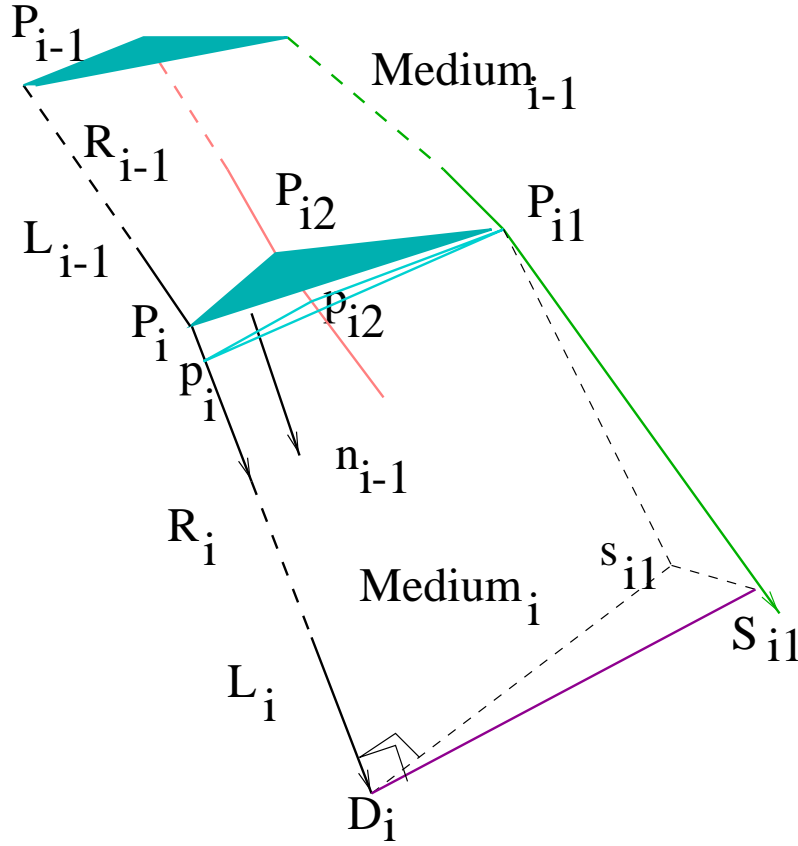

Figure 3.5: **Recursive Relations**

Figure 3.5 shows the interface between i-th and the (i-1)-th medium. Just for notational convenience, the interface between medium i and medium $i-1$ is denoted by triangle $\Delta P_i P_{i2} P_{i1}$, while the normal is $n_{(i-1)}$. There is no confusion. For example the interface between Medium 1 and 2, would be called

$\Delta P_2 P_{22} P_{21}$, same as $\Delta A A_2 A_1$ in earlier section (Figure 3.3), while it has normal n_1. The rationale behind such nomenclature is that the unshaded triangle just underneath, perpendicular to the ray $\mathbf{R_i}$ would be correspondingly called $p_i p_{i2} P_{i1}$. This is appropriate because it is inside the Medium i and not (i-1). At the point of interest in Medium i, D_i, the area perpendicular to the ray is $D_i s_{i1} S_{i1}$.

Similar to the discussion in the earlier section, we can arrive at the following relation.

$$
\begin{aligned}
SF_2 SF_3...SF_i &= \sqrt{\frac{\Delta a a_2 A_1}{\Delta D_i s_{i1} S_{i1}}} \sqrt{\frac{\cos\theta'_{23}}{\cos\theta_{23}} \frac{\cos\theta'_{34}}{\cos\theta_{34}} ... \frac{\cos\theta'_{(i-1)i}}{\cos\theta_{(i-1)i}}} \\
&= \sqrt{\frac{\Delta p_2 p_{22} P_{21}}{\Delta D_i s_{i1} S_{i1}}} \sqrt{\frac{\cos\theta'_{23}}{\cos\theta_{23}} \frac{\cos\theta'_{34}}{\cos\theta_{34}} ... \frac{\cos\theta'_{(i-1)i}}{\cos\theta_{(i-1)i}}} \quad (3.24)
\end{aligned}
$$

where $\theta_{(i-1)i}$ and $\theta'_{(i-1)i}$ are the incident and refractive angles at the interface between Medium i-1 and i.

The area at the numerator has been derived already in the last section. We refer to Equation 3.14.

To derive the general area at the point $\mathbf{D_i}$, $\Delta D_i s_{i1} S_{i1}$, we resort to recursive Equations. When going through the derivations for three-medium (in the appendix) it is evident that many of the vectors and lengths can be arrived at recursively. The generalized recursive extension to multiple layers is given in the appendix.

We can use the final result in Equation A.60 to arrive at the two lengths corresponding to the sides of the triangle $\Delta D_i s_{i1} S_{i1}$ as follows,

$$
\mathbf{D_i S_{i1}} = \delta_{\nu_1} \mathbf{P_i} - (\hat{\mathbf{R}}_\mathbf{i} \cdot \delta_{\nu_1} \mathbf{P_i}) \hat{\mathbf{R}}_\mathbf{i} + L_i(\delta_{\nu_1} \hat{\mathbf{R}}_\mathbf{i}) \quad (3.25)
$$

and

$$
\mathbf{D_i s_{i1}} = \delta_{\nu_2} \mathbf{P_i} - (\hat{\mathbf{R}}_\mathbf{i} \cdot \delta_{\nu_2} \mathbf{P_i}) \hat{\mathbf{R}}_\mathbf{i} + L_i(\delta_{\nu_2} \hat{\mathbf{R}}_\mathbf{i}) \quad (3.26)
$$

where ν_1 and ν_2 are the two variable angles about which the ray is differentially changed to obtain the flux-tubes. In the last section, ν_1 corresponded to ψ and ν_2 corresponded to η.

29

The various components of these equations such as $\delta_\nu \mathbf{P_i}$ can be obtained using the recursive relations derived in Equations A.57-A.59 in Appendix A.

Then, finally the area is given by,

$$Area \Delta D_i s_{i1} S_{i1} = |\mathbf{D_i s_{i1}} \times \mathbf{D_i S_{i1}}| \qquad (3.27)$$

Thus we can evaluate Equation 3.24 and substitute in Equation 3.23 to get the field f_{D_i}.

3.3   Losses

So far we have assumed a loss-less medium. In reality there are energy losses in the propagation of sound. There is loss due to absorption and back-scattering within medium. We can lump these two effects into a bulk attenuation coefficient characteristic of the medium. The attenuation is an exponential function of the product of this coefficient and the path-length traversed in the each medium. Section 2.1.5 has some details on the absorption loss. The attenuation coefficient in general is a function of frequency [1]. The frequency dependence is linear for muscle and is specified in db/cm/MHz. Fat (like water) has very low attenuation coefficient but the frequency dependence is not linear but quadratic. Bone is highly attenuative.

There is another frictional loss - viscosity. However, we can ignore this loss in comparison to other phenomenon for the soft-tissues involved. In this work we ignore this effect.

3.4   Extension to Broad-band Pulses

So far we derived the field for monochromatic waves. In reality the transducers emit broad-band pulses. If we can measure the emitted pulses in advance or can model them in some way (for example using KLM modelling [10]), we can simply use the amplitude and phase factors obtained here to get the output for broad-band pulses . If we do not consider the distortion due to frequency-dependent attenuation, then the result is straightforward. The amplitude factors derived here are independent of frequency [2]. Hence

---

[2] The refractive index of the media for ultrasonic applications is virtually independent of frequency. Unlike optics, dispersion is negligible for the frequency-range [1]

the amplitudes just weight the emitted pulses and the phases provide the delays. This is true for low-attenuation medium such as water, fat etc.

Next we can take into account the attenuation to a first approximation. We can consider that the attenuation at the center-frequency is a good representation of the attenuation coefficient across the bandwidth. In this case, we could still add (interfere) the pulses undistorted. We just need to multiply another attenuation factor obtained with the value of frequency at the center-frequency of the pulse, on top of the intrinsic propagation-amplitude calculated here (due to boundary-conditions and spreading-factor). This approach suffices for most cases.

Finally, we can incorporate the true frequency dependent attenuation across the pulse's bandwidth - if we do the analysis in the frequency domain. For this case, amplitudes derived here and phases would be incorporated in the frequency domain for each ray and then the inverse Fourier transform gives the received pulse in time-domain, appropriately distorted by the attenuation coefficient.

Chapter 4

Ultrasound Field Propagation For a Special Case

In this chapter the goal is to derive the closed form equation for the the received echoes from a reflective media under two intermediate layers. This case is of special interest to us because it could be an useful tool for tracking the skeletal bone of a patient (through intervening layers of fat and muscle) intra-operatively. A potential application is accurate intra-operative registration with pre-operative CT data.

In this chapter we show that this particular case of reflection under two layers essentially reduces to the case of propagation through three media and therefore the results arrived at in the last chapter can be used.

4.1 Derivation of Field

In the following section we derive the received field amplitude and phase for the case of reflection off a interface under two-layers, when the incident field is a monochromatic spherical wave. As in the last chapter, we assume that the interfaces are arbitrary shaped but, locally planar to each individual ray. The ray-tracing approximation is assumed, which essentially means that the thicknesses of the layers has to be large in comparison to the wavelength.

4.1.1 Field received from a reflective layer under two intermediate layers
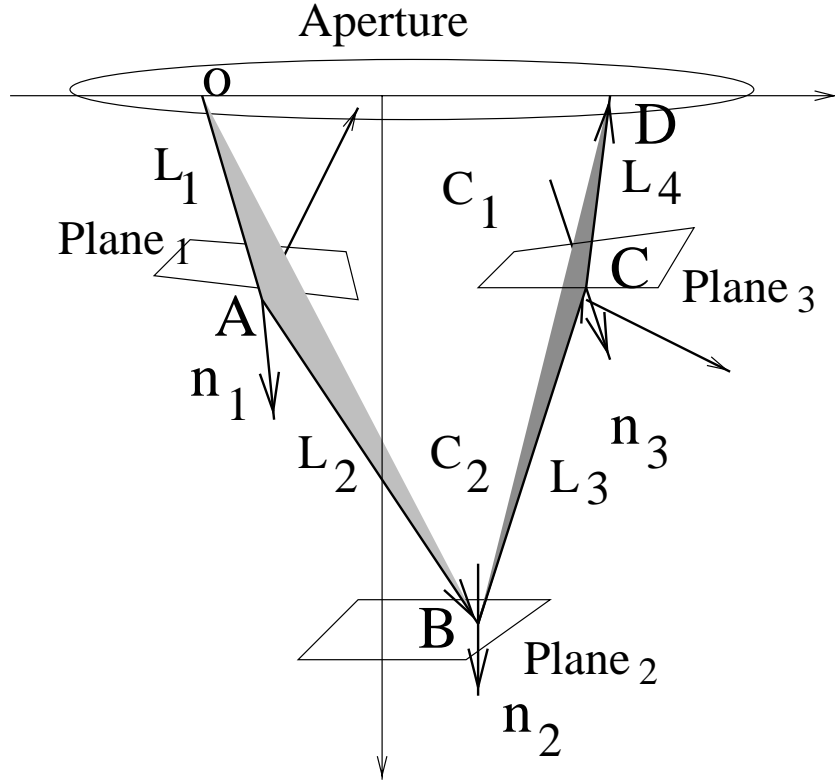

Figure 4.1: **Ray Skeleton For Analysis**

The main skeleton of rays we need to consider are given in Figure 4.1. At a later section (Section 4.1.2) we give the reasons for this. At this point it suffices to say that for example, when we are considering the boundary conditions at C, we need not consider the incident field at C direct from the source O. That field belongs to another skeleton and is taken care of when we process that. Plane 1 and Plane 3 (the dimensions are exaggerated here for convenience) are polygonal sections of the first interface. Plane 2 is the reflective surface. The normals of these planes are $\mathbf{n_1}$, $\mathbf{n_2}$, $\mathbf{n_3}$ all of which could be in general positions (and not necessary aligned perpendicular to the aperture). The ray O-A-B-C-D, is the main "skeleton" to be considered

here for analysis. The segments OA and CD are in the first medium (with propagation velocity C_1) and AD and BC are in the second medium (with propagation velocity C_2). The shaded regions indicate that one half (OAB) of the set of rays is in a different plane than the other half (BCD). OA, $\mathbf{n_1}$ and AB are coplanar (by Snell's Law), while BC, $\mathbf{n_3}$ and CD form a different plane.

The incident wave at A (Figure 4.1) is a spherical wave, the outgoing wave is distorted in shape due to refraction. The subsequent reflection at B does not change the waveform further (under ray-tracing approximation). The path ABC is entirely in the second medium. Hence we can reflect ray BC about the Plane 2, refer to Figure 4.2 and imagine it as continuing along AB. Then the CD part can also be reflected about Plane 2, but there is a change in the waveform again due to transfer to another medium again (medium 1).

The equivalent picture of the skeleton is given in Figure 4.2, where Plane $3'$ is the reflected plane and normal about the plane $\mathbf{n_3'}$ is the normal $\mathbf{n_3}$ reflected about $\mathbf{n_2}$. C' and D' are points C and D, reflected about the Plane 2. We are interested in figuring out the field at the point D', which represents the equivalent point back at the aperture. Note that the length OA and $C'D'$ are in first medium here while ABC' is in second.

We see that this is the same three-medium case considered in the last chapter, Figure 3.1, except in this case, Medium 3 is the same as Medium 1. An important difference is that we have an additional factor $R(\theta_I)$ in Equations 3.7 and 3.10 corresponding to the reflection at the second interface (plane B in Figure 4.2). This is a function of the incident angle θ_I. For a perfect reflector, this factor is unity. There are other obvious nomenclature differences, such as $L_2 + L_3$ is the segment of $\mathbf{R_2}$ in the second medium, and was called L_2 in the last chapter.

4.1.2 Independence of one ray-skeleton from another

In this section we explain why we can consider the ray-skeletons shown in Figure 4.1 independently.

Here we consider the point C in Figure 4.1, for the explanation, but similar arguments apply to point A as well.

Let us consider the point C and all the waves incident on it from the source O as well as from below, after reflection at the bone. This is shown in Figure 4.3. In this figure the solid lines represent the waves for the skeleton
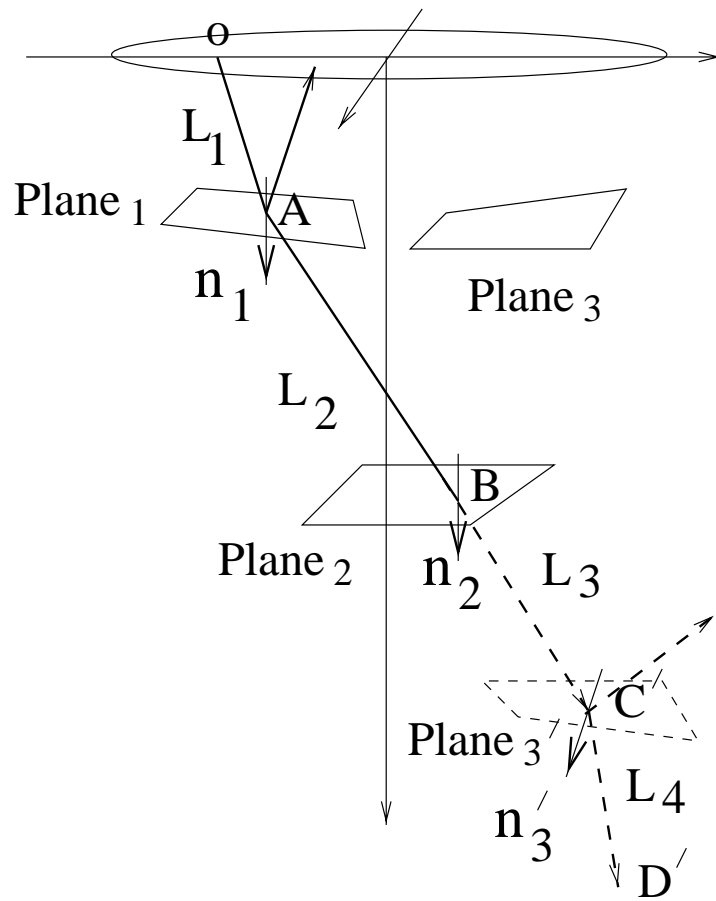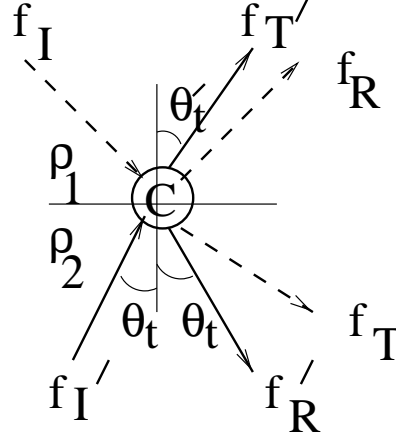
Figure 4.2: **Equivalent Ray Skeleton**

Figure 4.3: **Incident, Reflected and Refracted waves on point C**

considered in Figure 4.1 while the dotted lines incident wave direct from the source (which starts another skeleton at C). f_I', f_R', f_T' denote the incident, reflected, refracted velocity potentials from below, and f_I, f_R, f_T are those from above.

For an incident plane wave, continuity of the pressure and normal component of velocity at a planar interface gives the reflected plane wave (angle of reflection = angle of incidence) and the refracted plane wave (snell's law) as derived in many books [2, 9] to cite a few. Now for the spherical wave, under ray-tracing approximations, we can apply the boundary conditions ray-by-ray to obtain the reflected, refracted rays, as was done for the analysis in [2]. This is because the ray-tracing approximation essentially means that a component plane wave (at an angle θ) composing the spherical wave is effective only locally, around the ray (at an angle θ). This was discussed in Section 2.2.2.

Now we refer to Figure 4.3. First for each set of waves, f_I, f_R, f_T and f_I', f_R', f_T' by themselves have to satisfy the boundary conditions. This can be seen simply as follows. If for example we could block out the incident ray from above, the set of rays f_I', f_R', f_T' (shown by the solid-rays) are by themselves and have to satisfy the boundary conditions.

Hence by continuity of pressure condition, we would get, the following two equations, as shown below,

$$\rho_2(f_I + f_R) = \rho_1 f_T \tag{4.1}$$

and,

$$\rho_1(f_I' + f_R') = \rho_2 f_T' \tag{4.2}$$

Then, we add LHS of Equation 4.1 to RHS of Equation 4.2 and also add RHS of Equation 4.1 to LHS of Equation 4.2, and equate the sums, to get,

$$\rho_2(f_I + f_R + f_T') = \rho_1(f_I' + f_R' + f_T) \tag{4.3}$$

Which essentially says that for the set of six rays in Figure 4.3, the boundary condition is satisfied, that is the total potential at the top $(f_I + f_R + f_T')$ is related to the total potential at the bottom $(f_I' + f_R' + f_T)$ with the inverse ratio of the density.

Chapter 5

Experimental Results with Phantom and Comparison with Simulations

We have performed validation experiments for the forward model for the special case considered in the last chapter. We use "fat" and "muscle" mimicking phantoms. These physical objects designed from water-agar-gel mixtures mimick some ultrasound characteristics (such as propagation velocity) in human fat and muscle. We also used a steel-block about 5 cm thick. We place the phantoms on top of the steel-block and obtain the pulse-echoes from the fat-muscle interface as well as the muscle-steelblock interface. We simulate the same conditions and compare the experimental results with the simulations. For the purpose of simulations, we use the values for the velocity, density and the attenuation coeficient of the phantoms, that the manufacturers provide us with. We assume that the steel-block is a perfect reflector.

In this chapter, we first explain the experimental procedure in detail. We also explain how we obtain the transducer pulse needed for our simulations. We then compare the experiments with the simulation result.

5.1 Experimental Procedure and Equipment Description

To obtain coupling between the phantom layers we wet them with water. Then we stack on the steel-block so that the muscle-phantom lies on the steel-block and the fat-phantom on top of the muscle. The purpose is to create a highly reflective interface under two layers (fat and muscle).

The ultrasonic transducer used is a 7.5 MHz, single element circular aperture transducer. We use a RiTec control box with variable amplitude and frequency to trigger the transducer. We excite the transducer with a short square pulse of time-duration half of the time-period at resonance, (that is, $1/(2 \times 7.5)\mu s$ or about 67 nano-secs). We place the transducer over the fat-phantom and obtain the return-echoes. The echoes are captured, and filtered by a lowpass and a highpass filter. The lowpass filtered is set at 10 MHz. The highpass filter is set at 20 KHz, to remove the DC bias. The filtered signal is sampled at 25 MHz by an Analog to Digital Converter. A Sonix board is used for this purpose. The buffer length is 4096 samples. The Sonix board is triggered by a synchronizing trigger source from the control box.

The experiment on fat-muscle-steel is repeated twice.

A typical return-echo signal is shown in Figure 5.1.

In Figure 5.1, the first very high-amplitude echo at the beginning (near zero-time) is the echo off the interface between the transducer backing and the fat-phantom. The second echo is that from the fat-muscle interface. The next higher echo is from the muscle and steel-block interface.

5.2 Simulations and comparison with experiments

To be able to simulate the pulse-echo mechanisms, we have to determine the transducer pulse first. The first pulse echoed from the backing would have been a good candidate but its high amplitude saturated the electronics in the control-box. Hence, the pulse appears chopped off and is not useful. In the present work, we do an additional experiment to determine the pulse. We obtain an echo from the steel-block, under-water, placed far away (about 5 cm) from the transducer. This is to make sure that the delays experienced by

Sample Experiment

Echo off (1) backing, (2) fat–muscle and (3) muscle–fat interfaces
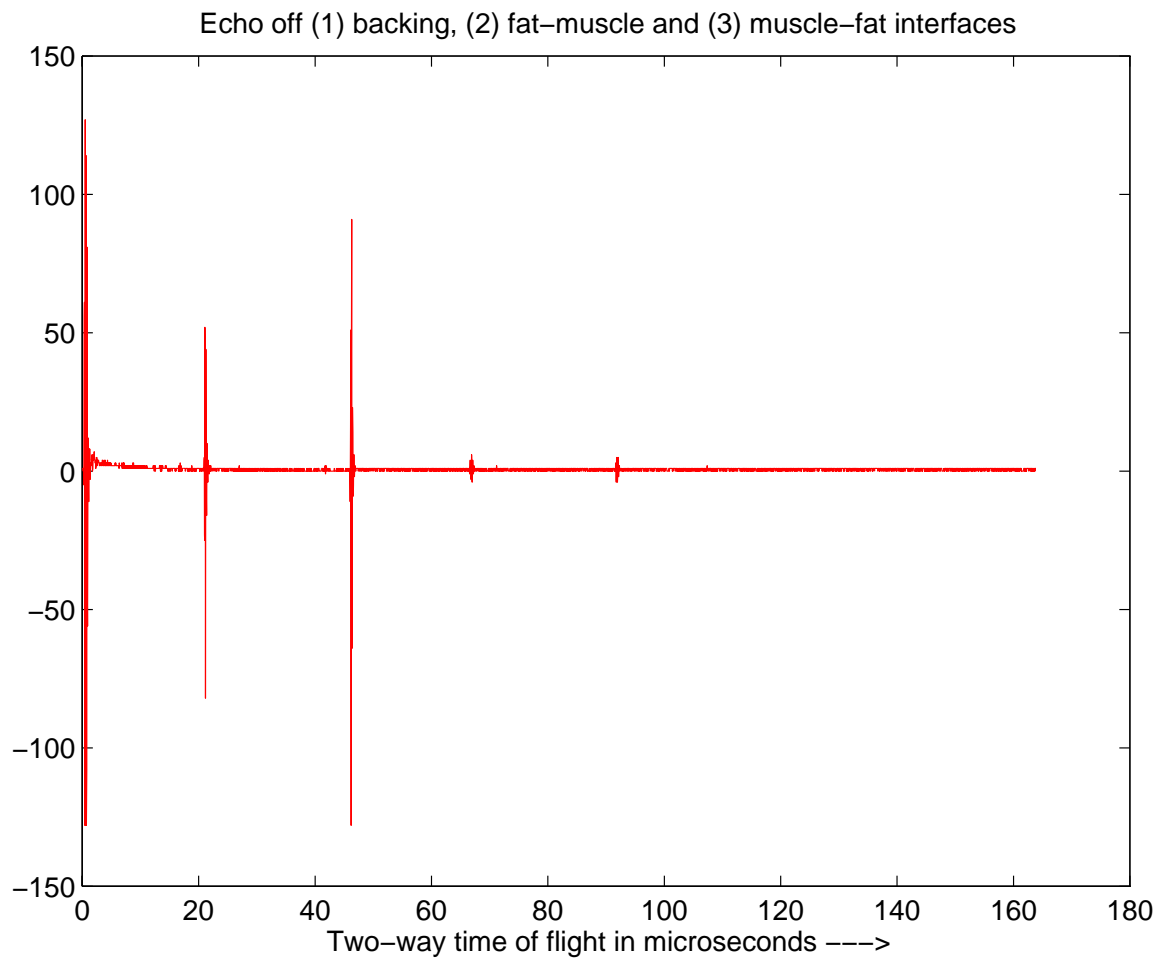

Figure 5.1: **Sample Experiment**: Echo Signals from fat-muscle and muscle-steel interface

the emitted-pulse in going through the ray-paths are roughly the same. This is true if the distance from the transducer is far enough away in comparison to the aperture diameter and the wavelength [1]. This type of experimental determination of pulse is a standard method to measure the pulse when the transducers are tested by designers [2]. The pulse obtained is observed to be nearly a Gaussian. We fit a Gaussian curve using simplex algorithm. The parameters fitted to the Gaussian are amplitude, mean, standard deviation, and the center frequency of modulation. In the next section we show the results.

5.2.1   Experimental determination of Transducer pulse

Figure 5.2 shows the pulse we obtained. We maximize the return echo from the steel-block under water, about 5 cm from the 3 mm diameter transducer.
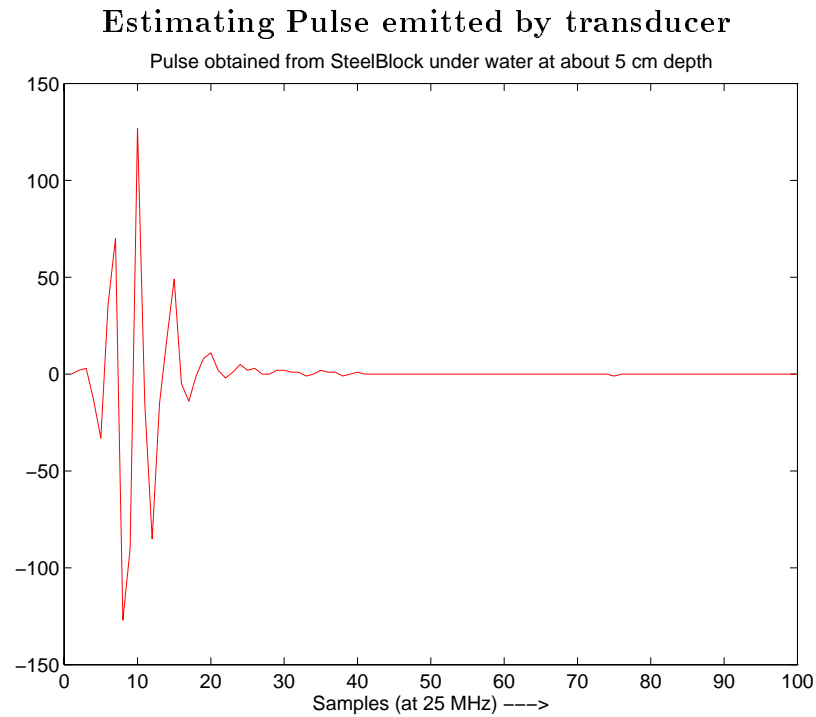
The parameters of the Gaussian fitted to the experimental data is tabulated.

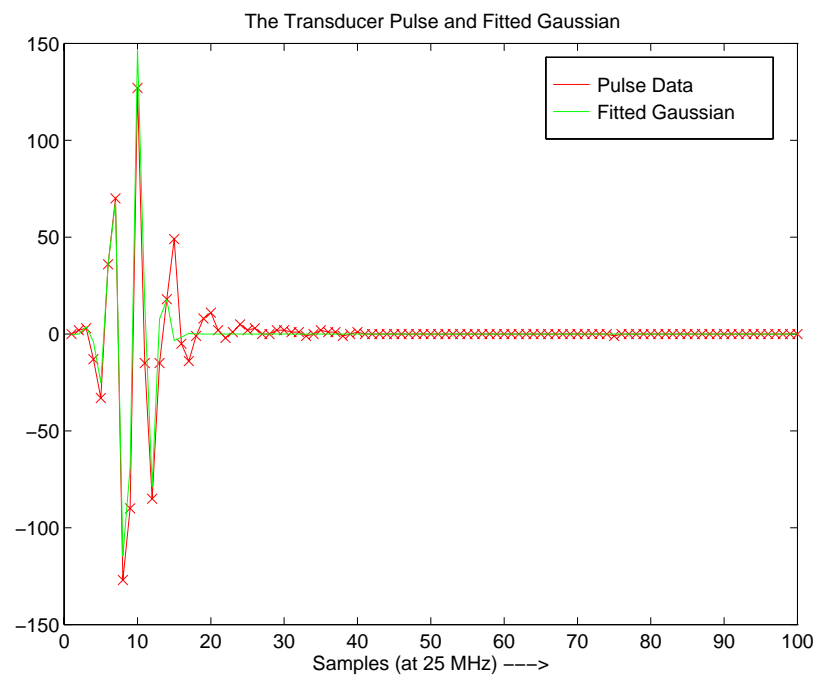| Parameters of the fitted Gaussian	
	Parameters
Amplitude	161.4234
Mean (samples)	9.2562
Sigma (samples)	2.2884
Frequency (MHz)	6.8748

It is noted that the pulse obtained by this experiment give estimates of the transducer-pulse only to a scale. Therefore, we do not know the exact amplitude scaling of the pulse just emitted out of the transducer. When comparing simulations and experiments we use a scaling factor that matches one of the echoes in the simulated and the experimental signals. Then we can compare the amplitude and the shape of the other one.

---

[1]Strictly speaking, this experiment will give not give just the pulse emitted from the transducer but that pulse, convoluted twice (forward and return) with the transducer impulse response. However, that does not pose a problem and is in fact necessary. Because all the echoes we are going to subsequently measure by the transducer are also going to be convoluted twice with this impulse-response. Hence, we do need the emitted pulse after twice convolution with the transducer impulse response.

[2]personal communication, Mr. Xue, Advanced Devices.

Estimating Pulse emitted by transducer

Pulse obtained from SteelBlock under water at about 5 cm depth

(a) Pulse from Steel-block

The Transducer Pulse and Fitted Gaussian

(b) Pulse compared to a best fit Gaussian.

Figure 5.2: **Transducer Pulse and the best fit Gaussian used for simulations**

5.2.2 Parameters used in Simulation

A Gaussian pulse is used for simulation, with parameters as listed in the table in last section.

The next table shows the medium parameters used for the simulations. The phantoms are designed as flat slabs with designated thicknesses. So the geometry of the phantom surfaces are assumed planar and parallel to the aperture for simulation purposes. The same is true for the steel-block surface as well. The steel block is assumed a perfect reflector.

Parameters used in simulations		
Parameters	Phantom 1 (fat)	Phantom 2 (muscle)
Relative density (wrt water)	1.010	1.041
Velocity in $mm/\mu s$	$C_1 = 1.508$	$C_2 = 1.582$
Attenuation in $db/cm/MHz$	0.067	0.188
Thickness in mm	15	20

The attenuation (due to loss) parameter is converted to db/cm by multiplying the listed attenuation values with the center frequency of the pulse, 6.8748 MHz. The attenuation (in db) is obtained by multiplying the individual ray lengths in each medium by the given attenuation factor, in the simulator. The factor is (after appropriately powered) multiplied to the intrinsic propagation amplitude calculated for each ray.

The simulator is written in C.

5.2.3 Simulation Results and Comparison with Experiments

We compare the experiments with simulation results. For purpose of comparison we show the simulated echoes superposed on the experimental echoes. Additionally, we calculate relevant ratios and summarize them in a table. The experiment is repeated twice.

The Figures 5.3-5.5 show the first experimental results and the simulation.

Since we do not know the amplitude scale of the emitted pulse, for purpose of comparison, we have scaled the simulation data so that the RMS amplitude of the first echoes match for the experiment and the simulation. Then we compare the second echo in amplitude.
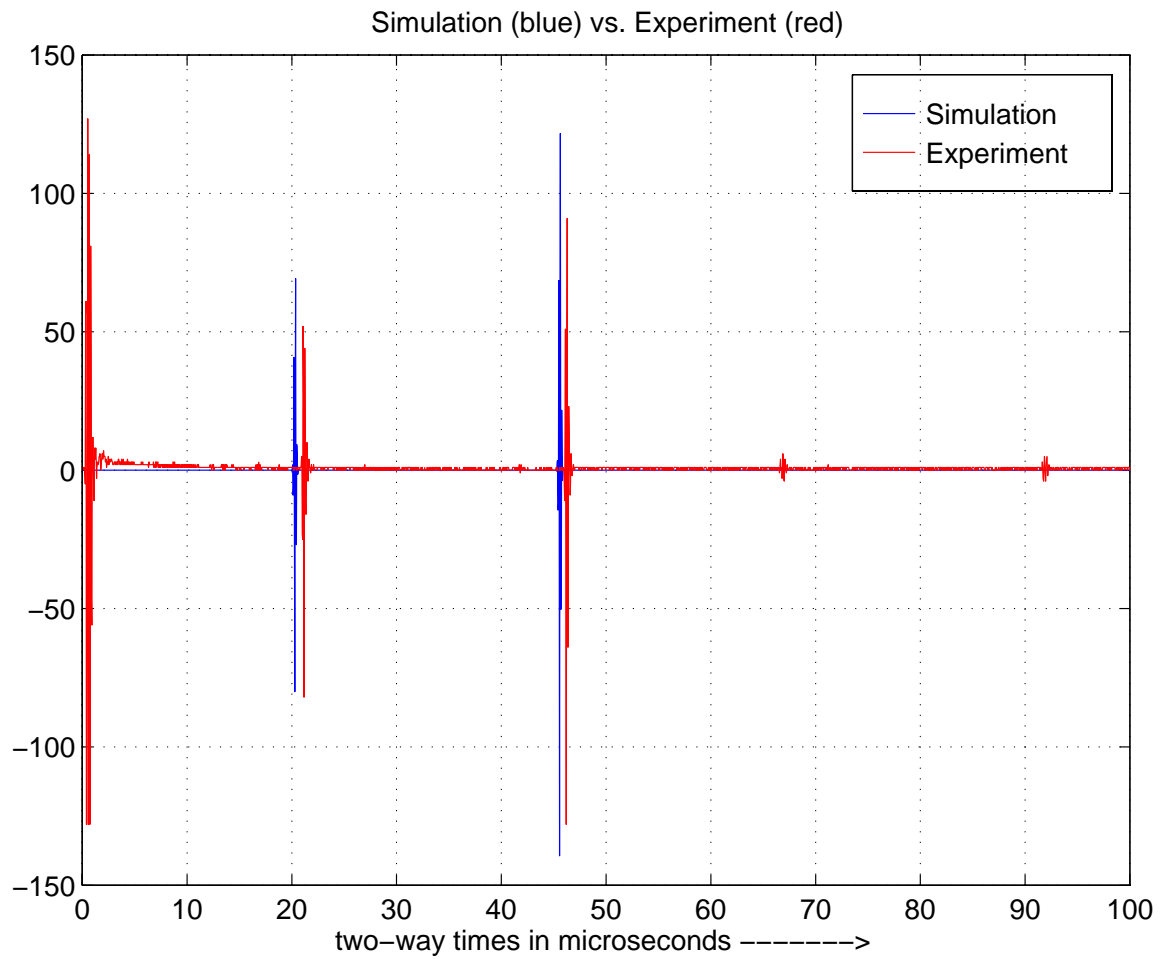
Comparison of Experiment 1 with Simulations

Figure 5.3: **Experiment 1**: Comparison of Experiment and Simulation

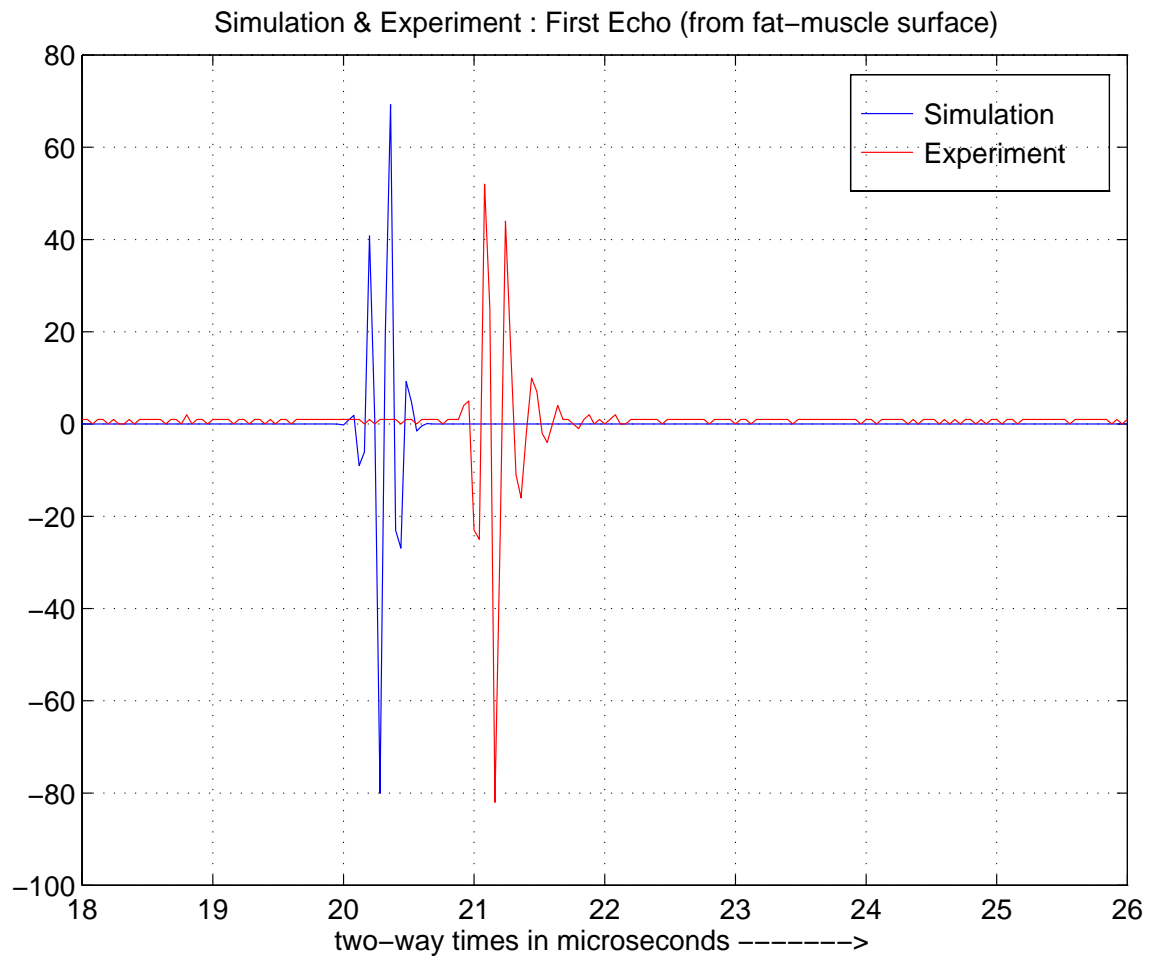## Comparison of Experiment 1 with Simulations

Figure 5.4: **Experiment 1**: Comparison of close-up of the first echo

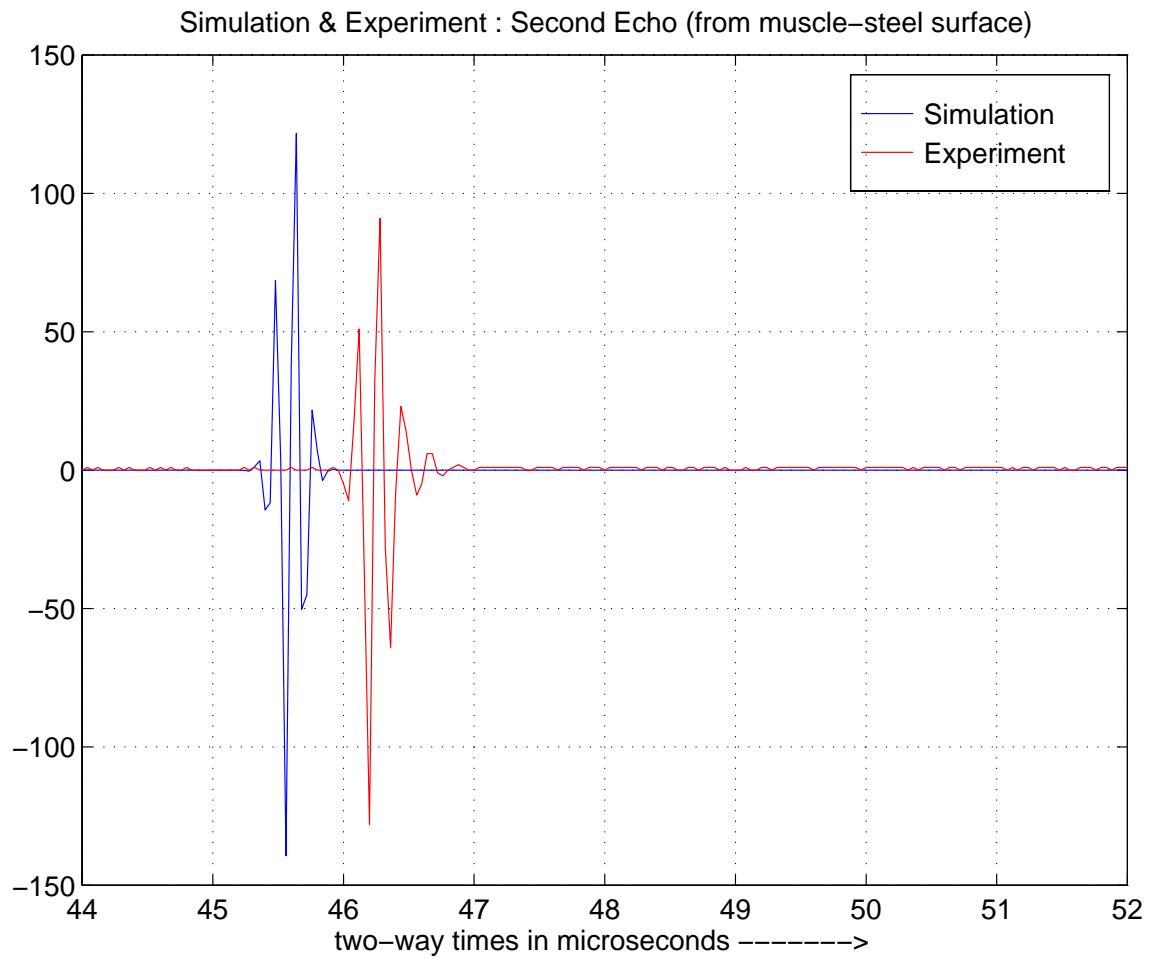# Comparison of Experiment 1 with Simulations

Figure 5.5: **Experiment 1**: Comparison of close-up of second echo

The plot in Figure 5.3 shows the echoes off the fat-muscle and the muscle-steelblock interfaces. The red plot shows the experiments and the blue plot simulations. In all these figures, the first echoes of the experimental (red) plot and the simulation (blue) plot are deliberately matched in amplitude. That is, the simulation plot has been scaled such that the square root of the sum of squares of the echoes match for the two cases. The RMS amplitude ratio of the simulated second echo to the experimental one is calculated and tabulated in the summary table.

The Figures 5.4-5.5 show the echoes close-up. There are small delay-errors, in fractions of mm, of the echoes. We also tabulate these shifts in mms. For the first pulse, the distance shifts, δx_1 in terms of the (two-way) time mismatch δt_1 calculated from the simulated and the experimental echo, is given by $\delta x_1 = C_1 \delta t_1 / 2$. For the second echo, after a few calculations the shift in mm is $\delta x_2 = C_1 \delta t_1 / 2 + C_2 (\delta t_2 - \delta t_1)/2$. These values are tabulated in the summary table.

Figures 5.6-5.8 shows the echoes and their close-ups for the second experiment. The amplitudes and shift-errors for this set is also tabulated in the next section.

Summary of Results

We summarize the comparison of experiments and simulations in following table.

Comparison with Experiment 1 and Simulation	
[RMS Echo1]/[RMS Echo2] - simulation	0.5670
[RMS Echo1]/[RMS Echo2] - experimental	0.6378
[Experiment Echo2]/[Simulation Echo2]	0.8890
Echo 1 shift-error (δx_1)	-0.6334 mm
Echo 2 shift-error (δx_2)	-0.5068 mm

The first two entries shows the relative RMS amplitude between the first echo and the second echo for the simulation data and the experimental data respectively. Ideally these ratios should have been the same. The next entries gives some more comparisons. The third entry is the amplitude ratio of the second echo between the experimental to the simulation data. This has been obtained after we scaled the simulation so that first echoes match. Note that

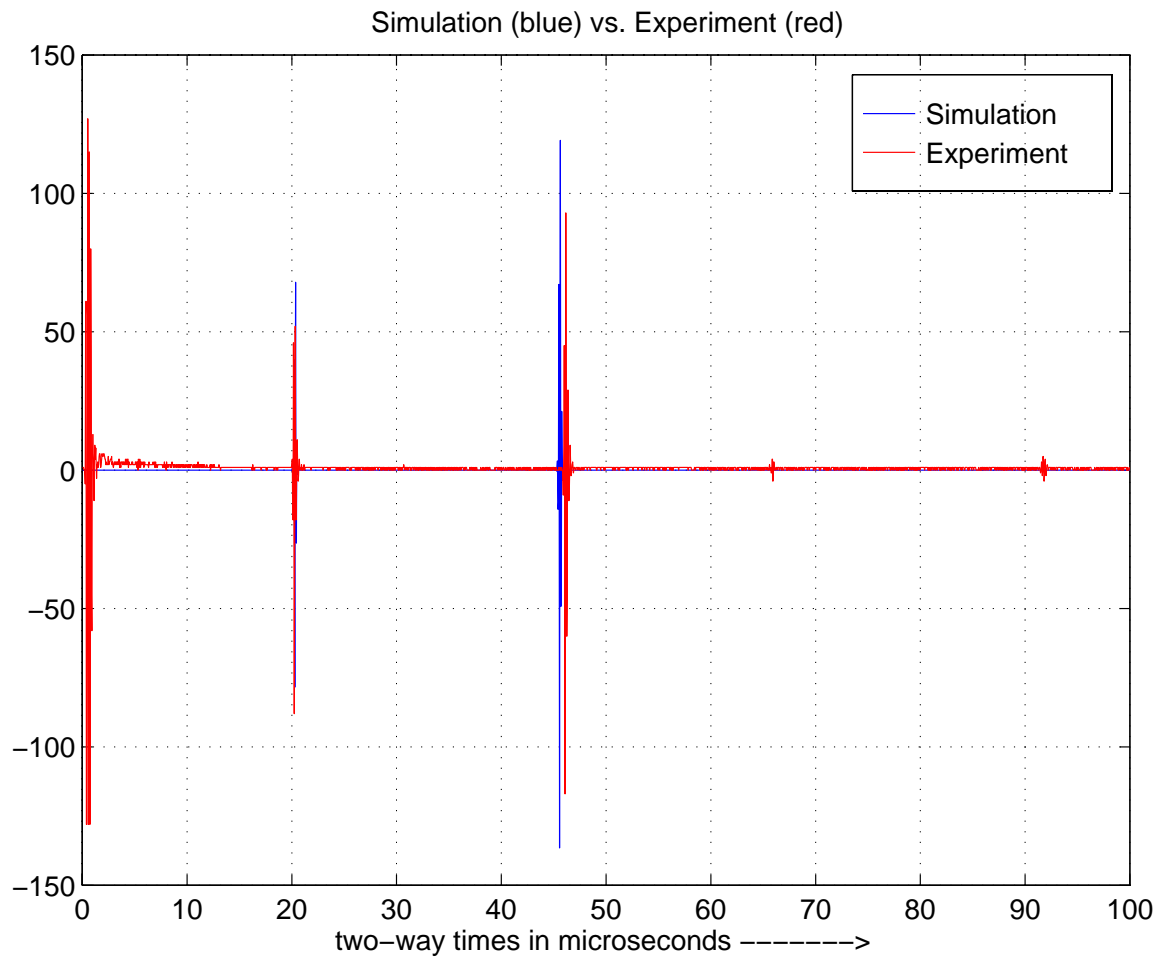# Comparison of Experiment 2 with Simulations

Figure 5.6: **Experiment 2**: Comparison of Experiment and Simulation
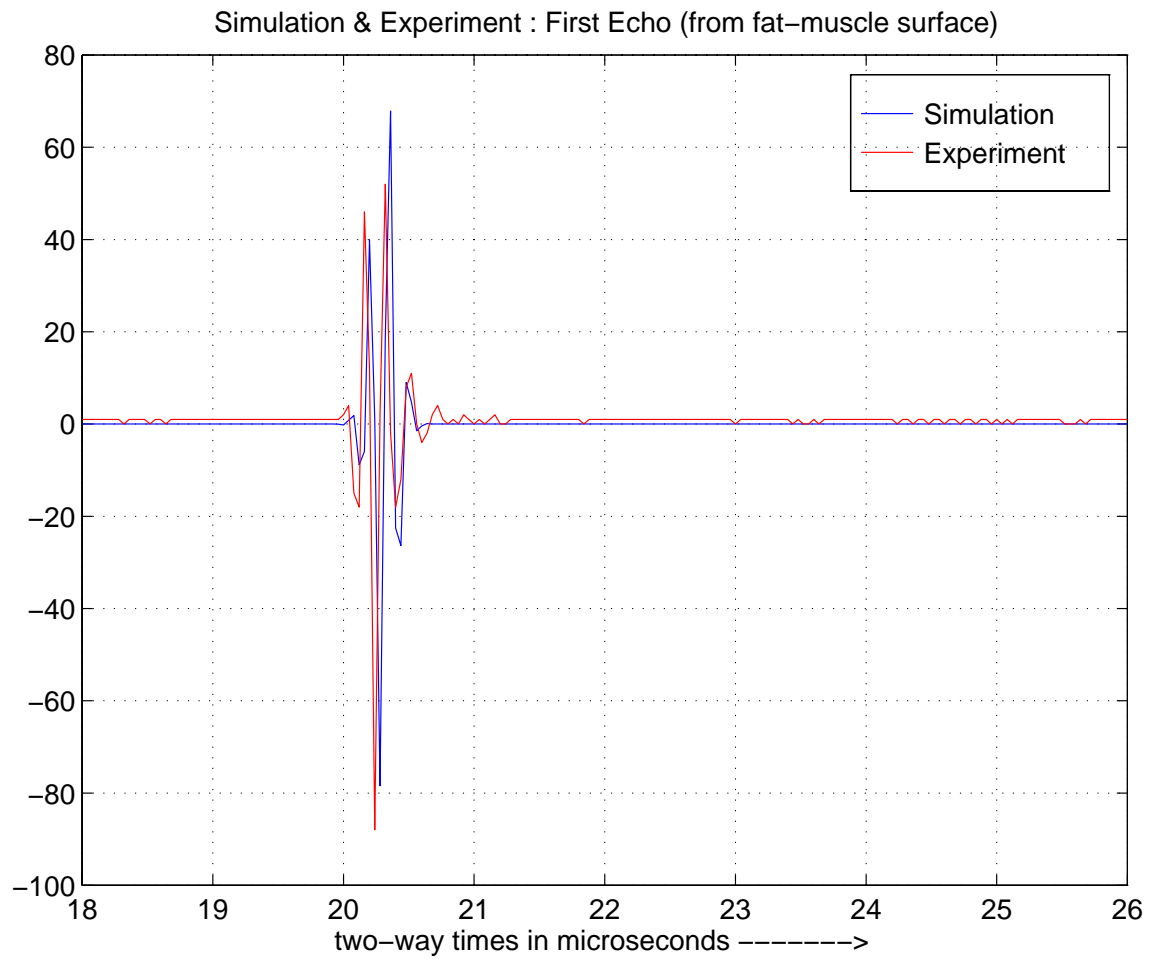
Comparison of Experiment 2 with Simulations

Figure 5.7: **Experiment 2**: Comparison of close-up of the first echo

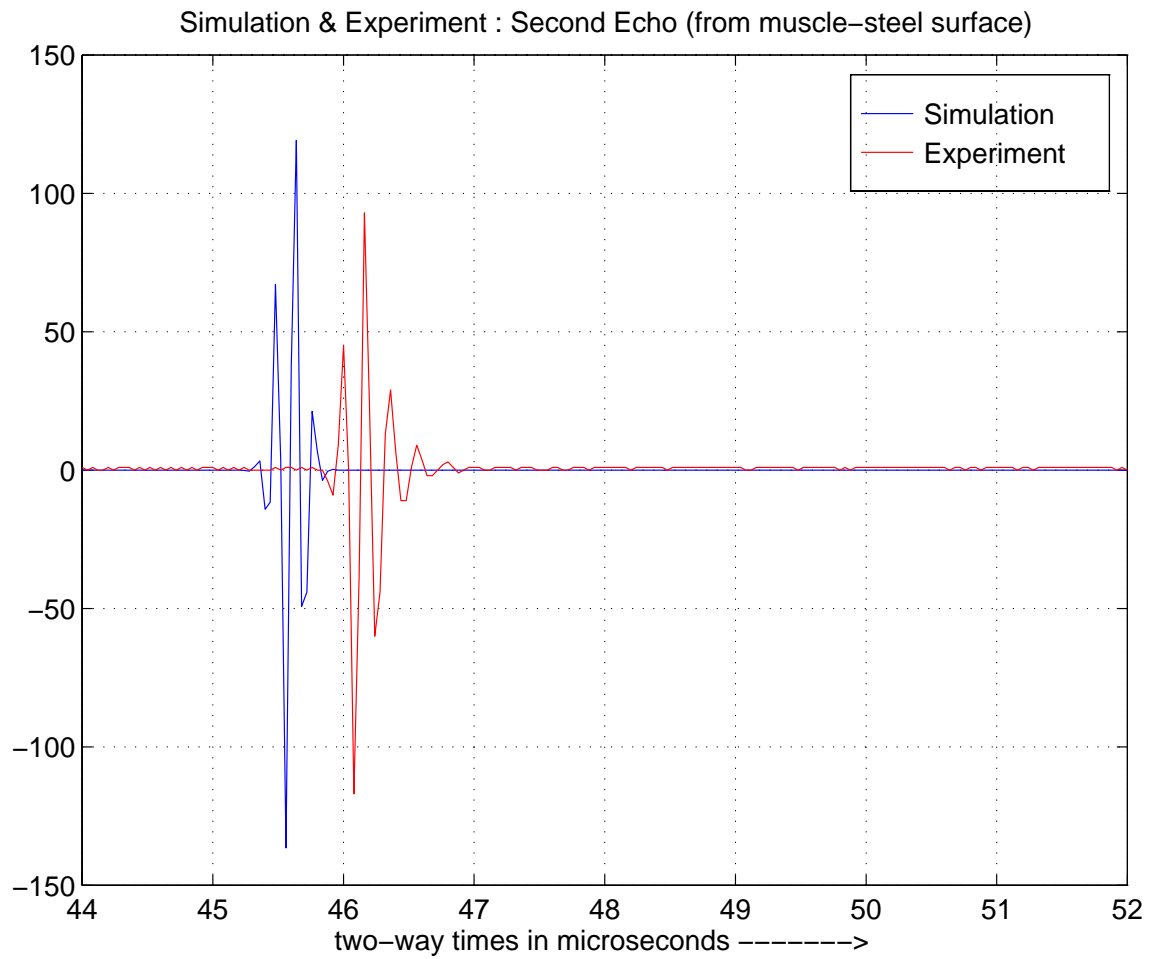# Comparison of Experiment 2 with Simulations

Figure 5.8: **Experiment 2**: Comparison of close-up of second echo

this number (ideally unity) also gives us the ratio (or discrepancy) between the numbers in the first two entries. The last two entries give the shifts-errors (in mm) between the echoes of the experiments and simulations.

A second table presents results for the second experiment.

Comparison with Experiment 2 and Simulation	
[RMS Echo1]/[RMS Echo2] - simulation	0.5670
[RMS Echo1]/[RMS Echo2] - experimental	0.6487
[Experiment Echo2]/[Simulation Echo2]†	0.8741
Echo 1 shift-error (δx_1)	0.0603 mm
Echo 2 shift-error (δx_2)	-0.4459 mm

5.3 Conclusions

The amplitude matches are fairly good. The echoes from the steel-block being slightly lower than expected could be a result of the fact (1) that there is a small amount of transmission into the steel-block whereas we assume that the steel-block is a perfect reflector in the simulations (2) there is an angular sensitivity of the transducer. Additionally there is a frequency-varying attenuation. There is small but visible amount of downshift in frequency in the second echo because the higher frequencies are attenuated more. For the simulation we took the attenuation at the center-frequency.

There are small relative-shifts of the pulses. However, these shifts are within the design errors of the phantoms. The phantom thicknesses are correct to within a mm. We measured the phantoms with calipers at various spots and there was some variation (< 1 mm).

Chapter 6

Conclusions

In this work we have presented closed-form derivation of ultrasound field under ray-tracing approximations for commonly occuring cases. We first show by some preliminary calculations that the ray-tracing approximation is not very restricting. Then we go on to discuss other assumptions.

6.1　How restricting is ray-tracing approximation ?

We discuss the applicability of the ray-tracing conditions. A check on the limits of ray-tracing can be done using Equation 2.15 for the field under two-layers for the nominal values of parameters for fat and muscle obtained from [18], for imaging with a 3.5 MHz transducer. With $C_1 = 1.48\frac{mm}{\mu s}$, $C_2 = 1.57\frac{mm}{\mu s}$, (that is $n = \frac{1.48}{1.57} = 0.9427$), we would get,

$$z >> 0.2017mm \qquad (6.1)$$

That is, for depths sufficiently more than $0.2017mm$ from the boundary, the ray-tracing approximation is valid. This factor is inversely proportional to the frequency used. For example, at 7.5 MHz, we need a depth more than $0.0941mm$ making the condition even less restricting.

6.2 Other assumptions

The main other physical approximations apart from ray-tracing is that of longitudinal propagation. However for soft-tissues, this assumption is not very stringent. Transverse or shear-waves are not transmitted very effectively through human soft-tissue [1]. However, for solid media such as bone, shear-waves are also important [1].

In the current model, the reflection off the different interfaces have been considered specular. This is generally true of interfaces between organs. However in some cases, there could be diffuse reflection as well [1].

We note that we ignored secondary and multiple levels of reflection off the interfaces because they would be highly attenuated because of large path-lengths and also have large delays. This is a standard assumption [3, 6, 19], etc.

Absorption and backscattering loss in the media has been considered, but for viscosity losses the wave-equation has to be modified further.

Finally, we have assumed each of the medium to be homogeneous. A more generalized model would take into account the within-tissue variations of density and velocity. The ray-tracing approach would be still valid. The rays would not be straight but bend within the medium. We also use a bulk-measure to account for the back-scattering due to scatter-centers inside medium. However there has been significant amount of work on explicit modeling of ultrasonic scattering [20, 21, 22, 23, 24], as well as the inversion [25, 26, 19, 27, 28]. However, all these are added at the expense of complexity. The magnitude of back-scattering effect is far smaller than the magnitudes of specular and diffuse reflections from interfaces of organs [1].

The current model of assuming layered homogeneous media applies well for a fairly wide cases, because the human body is layered with not so sig-

---

[1]For applications such as insonification through solids such as skull-bone etc, just longitudinal propagation is not valid and we need to adopt a more refined model to take into account shear-waves. More over the shear-wave and the longitudinal-waves cannot be analyzed independently, because the physical variables will have components due to both. For example, considering an isotropic, homogeneous medium which can support shear-waves as well as longitudinal-waves, the displacement vector $\mathbf{u}$ has a vector potential ψ as well as the scalar longitudinal potential ϕ. The displacement is given by [10], $\mathbf{u} = \nabla\phi + \nabla \times \psi$. Deriving wave-equations of the form in Equation 2.1 in ϕ as well as in ψ as given in [10] and solving for them, all the other physical variables such as displacement, stress, strain can be deduced from ϕ and ψ.

nificant variation of density, velocity of propagation within medium.

We can summarize the advantages of the model as follows. To a good first approximation it would model the effect of layered media for common cases where the layers are essentially homogeneous and support mainly longitudinal waves. Fat, muscle answer these criterion well. Hence as a good first approximation (neglecting the in-medium variations), we can apply this model. The layers should be more than orders of of mm thick when we use transducers of medium frequencies (1-10 MHz). The advantage of the ray-tracing approach is that it is highly parallelizable (each ray is independent of another) and could be potentially very fast. This factor is useful for real-time applications and is also essential if we attempt to invert the forward model.

It is a step forward from the state of the art scanner which uses a single longitudinal velocity for soft-tissue.

Bibliography

[1] J. A. Zagzebski, *Essentials of Ultrasound Physics*. Mosby-Year Book, Inc, 1996.

[2] L. M. Brekhovskikh, *Waves In Layered Media*. Academic Press, 1980.

[3] L. Odegaard, S. Holm, F. Teigen, and T. Kleveland, "Acoustic field simulation for arbitrarily shaped transducers in a stratified medium," in *Proceedings IEEE Ultrasonics Symposium*, pp. 1535–1538, 1994.

[4] L. Odegaard, S. Holm, and H. Torp, "Phase aberration correction applied to annular array transducers when focusing through a stratified medium," in *Proceedings IEEE Ultrasonics Symposium*, pp. 1159–1162, 1993.

[5] D. A. Carpenter, D. E. Robinson, P. L. Ho, D. Martin, and P. Isaacs, "Body wall aberration correction in medical ultrasonic images using synthetic-aperture data," in *Proceedings IEEE Ultrasonics Symposium*, pp. 1131–1134, 1993.

[6] G. Kossoff, D. Carpenter, D. Robinson, D. Ostry, and P. Ho, "A sonographic technique to reduce beam distortion by curved transducers," *Ultrasound in Medicine and Biology*, vol. 15, no. 4, pp. 375–382, 1989.

[7] D. Carpenter, G. Kossoff, and K. A. Griffiths, "Correction of distortion in us images caused by subcutaneous tissues: Results in tissue phantoms and human subjects," *Radiology*, vol. 195, pp. 563–567, May 1995.

[8] S. Smith, G. Trahey, and O. V. Ramm, "Phased array ultrasound imaging through planar tissue layers," *Ultrasound in Medicine and Biology*, vol. 12, no. 3, pp. 229–243, 1986.

[9] A. D. Pierce, *Acoustics: An Introduction to Its Physical Principles and Applications.* McGraw Hill, Inc, 1981.

[10] G. S. Kino, *Acoustic Waves: Devices, Imaging, And Analog Signal Processing.* Prentice-Hall, Inc, 1987.

[11] J. W. Goodman, *Introduction to Fourier Optics.* McGraw Hill, Inc, 1968.

[12] P. M. Morse and K. U. Ingard, *Theoretical Acoustics.* McGraw Hill, Inc, 1968.

[13] G. P. Harris, "Review of transient field theory for a baffled planar piston," *Journal of Acoustic Society of America*, vol. 70, no. 1, pp. 10–20, 1981.

[14] G. E. Tupholme, "Generation of acoustic pulses by baffled plane pistons," *Mathematika*, vol. 16, pp. 209–224, 1969.

[15] D. A. Christensen, *Ultrasonic Bioinstrumentation.* John Wiley & Sons, 1988.

[16] A. Macovski, "Ultrasonic imaging using arrays," *Proceedings of the IEEE*, vol. 67, pp. 484–495, April 1979.

[17] E. B. Miller and F. L. Thurstone, "Linear ultrasonic array design for echosonography," *Journal of Acoustic Society of America*, vol. 61, pp. 1481–1491, June 1977.

[18] S. A. Goss, R. L. Johnston, and F. Dunn, "A comprehensive compilation of empirical ultrasonic properties of mammalian tissues," *Journal of Acoustic Society of America*, vol. 64, pp. 423–457, August 1978.

[19] E. J. Ayme-Bellegarda and T. M. Habashy, "Ultrasonic inverse scattering of multidimensional objects buried in multilayered elastic background structures," *IEEE Transactions on Ultrasonics, Ferroelectrics and Frequency Control*, vol. 39, pp. 11–18, January 1992.

[20] O. Buzma and R. Kuc, "Characterizing pulses reflected from rough surfaces using ultrasound," *Journal of Acoustic Society of America*, vol. 89, pp. 2519–2531, June 1991.

[21] J. Jensen, "A model for the propagation and scattering of ultrasound in tissue," *Journal of Acoustic Society of America*, vol. 89, pp. 182–190, January 1991.

[22] J. Jensen, "Deconvolution of ultrasound images," *Journal of Acoustic Society of America*, vol. 14, pp. 1–15, 1992.

[23] L. M. Hinkelman, D. Liu, L. A. Metley, and R. C. Waag, "Measurements of ultrasonic pulse arrival time and energy level variations produced by propagation through abdominal wall," *Journal of Acoustic Society of America*, vol. 95, no. 1, pp. 530–541, 1994.

[24] L. M. Hinkelman, T. L. Szabo, and R. C. Waag, "Measurements of ultrasonic pulse distortion produced by human chest wall," *Journal of Acoustic Society of America*, vol. 101, pp. 2365–2373, April 1997.

[25] Y. Li, "Phase aberration correction using near-field signal redundancy - part i: Principles," *IEEE Transactions on Ultrasonics, Ferroelectrics and Frequency Control*, vol. 44, pp. 355–371, March 1997.

[26] Y. Li, D. Robinson, and D. Carpenter, "Phase aberration correction using near-field signal redundancy - part ii: Experimental results," *IEEE Transactions on Ultrasonics, Ferroelectrics and Frequency Control*, vol. 44, pp. 372–379, March 1997.

[27] O. Haddadin and E. Ebbini, "Self-focusing arrays for imaging and therapy through inhomogeneous media," in *Proceedings IEEE Ultrasonics Symposium*, pp. 1563–1566, 1996.

[28] O. Haddadin and E. Ebbini, "Solution to the inverse scattering problem using a modified distorted born iterative algorithm," in *Proceedings IEEE Ultrasonics Symposium*, pp. 1411–1414, 1995.

[29] A. S. Glassner, *An Introduction to Ray Tracing*. London : Academic, 1989.

Appendix A

Derivation of Sides of Cross-sectional Triangles For Flux-Tube

In this chapter the goal is to derive the expressions of various differential vectors (and their lengths) in the different media. In the first section we consider the differential vectors by varying in the $d\psi$-direction. In a subsequent section we adapt these results for the $d\eta$-direction. Both these sections consider only three media. In the last section we find the recursive equations to extend to multiple media.

A.1 Differential vectors in $d\psi$-direction for three media

For convenience, we repeat Figure 3.3 in the main text here, shown in Figure A.1.

The eventual goal is to obtain the ratios of the areas orthogonal to the ray. In this appendix, we obtain the various sides of the relevant triangles in order to obtain these areas.

The analysis in this section corresponds to the vectors obtained by variation of the main-ray through angle $d\psi$ (shown in Figure A.2). The differentially shifted is in the plane of the z-axis and the original ray $\mathbf{R_1}$. We note that $\mathbf{R_1}$, $\mathbf{R_2}$ and $\mathbf{n_1}$ are coplanar. And the differentially shifted ray, $\mathbf{OA_1}$,
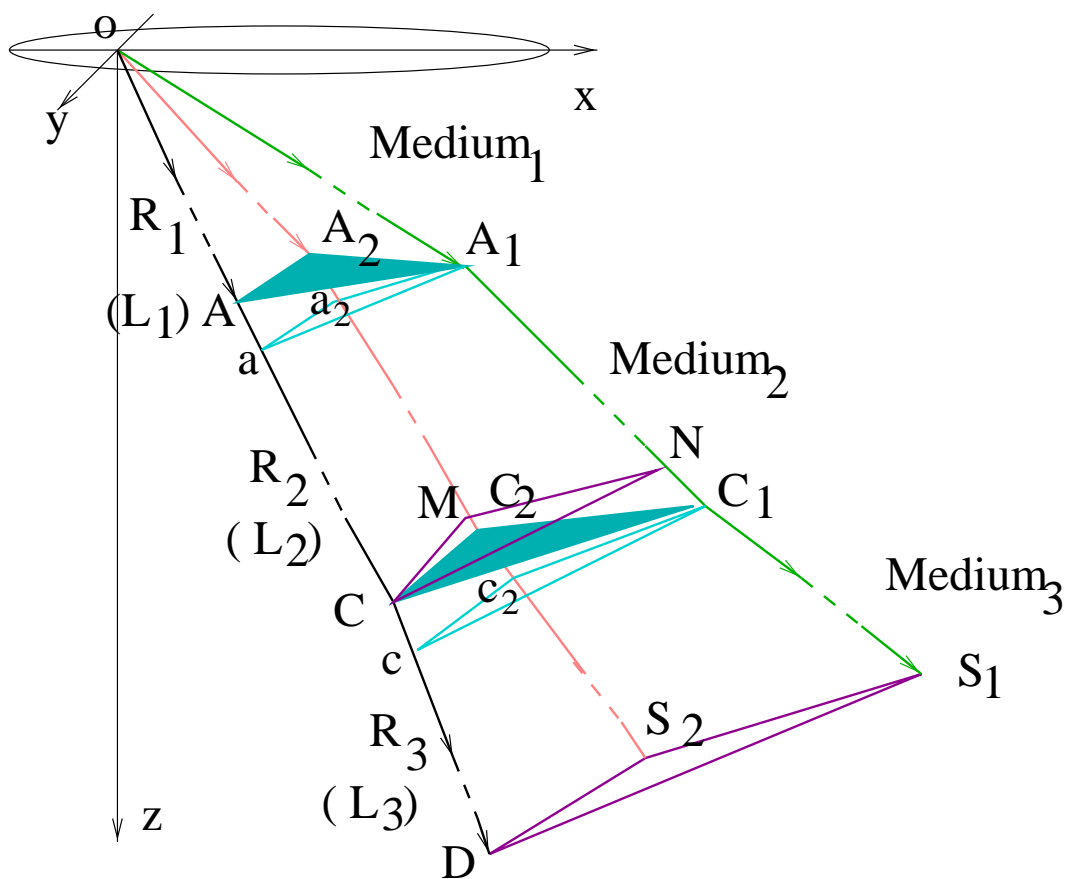
Figure A.1: **Areas of Energy Conservation**

$\mathbf{n_1}$ and refracted ray thereof $\mathbf{A_1 C_1}$ are coplanar. However, we cannot say the two refracted rays themseves $\mathbf{R_2}$ and $\mathbf{A_1 C_1}$ are not. This same observation holds in subsequent stages.
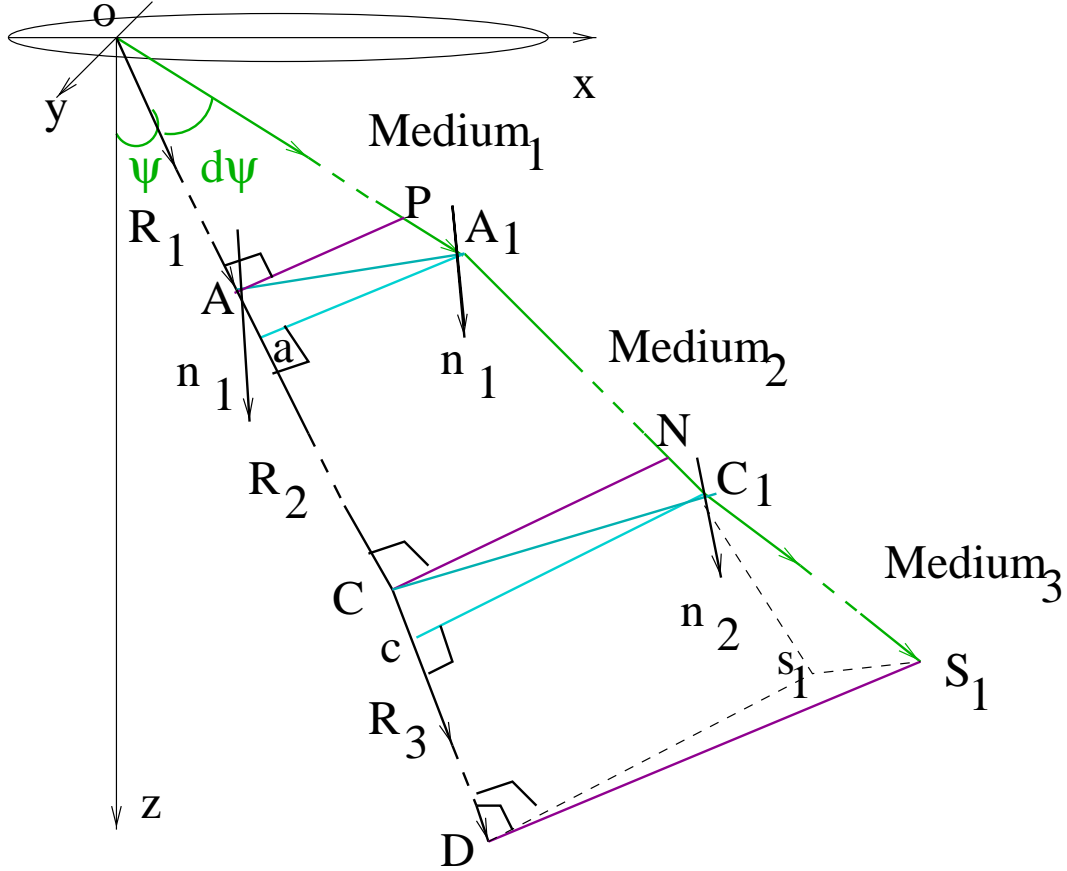
Figure A.2: **Calculation of Differential Vectors**

We want to derive the various differential lengths to the common measure $d\psi$, so that when considering ratios, this quantity is cancelled. Similar analysis holds for the vectors swept out by variation of main-ray through angle $d\eta$, in an orthogonal direction (not shown here for convenience). The equations would be the same in form, except that the variable is η and we want to reduce the various differential lengths to the common measure $d\eta$.

We are interested in the lengths perpendicular to the points just above the interfaces, vectors such as $\mathbf{DS_1}$, as shown in Figure A.2. Also the vec-

tors perpendicular to the rays just below the interfaces, ie, vectors such as $\mathbf{aA_1}, \mathbf{cC_1}$. We derive the vectors $\mathbf{aA_1}$ and $\mathbf{DS_1}$ because they are the most relevant in the main text. But their derivation, (specially that of $\mathbf{DS_1}$) shows how the vectors at any point can be arrived in general. This generalization and extension to multiple media is derived at another section.

The vectors that are needed in the main text are marked in boxes.

The vector $\mathbf{R_1}$ is given by

$$
\begin{align}
\mathbf{R_1} &= L_1 \hat{\mathbf{R}}_1 \tag{A.1} \\
&= L_1 \begin{pmatrix} \sin\psi\cos\eta \\ \sin\psi\sin\eta \\ \cos\psi \end{pmatrix} \tag{A.2} \\
&\tag{A.3}
\end{align}
$$

The "hat" over the vectors denotes unit-vectors.

The change in direction of $\mathbf{R_1}$ is given by,

$$
\begin{align}
\delta_\psi \hat{\mathbf{R}}_1 &= \frac{\partial \hat{\mathbf{R}}_1}{\partial \psi} d\psi \\
&= d\psi \begin{pmatrix} \cos\psi\cos\eta \\ \cos\psi\sin\eta \\ -\sin\psi \end{pmatrix} \tag{A.4} \\
&= (d\psi)\hat{\mathbf{x}}_{1\psi} \tag{A.5}
\end{align}
$$

where the unit-vector $\hat{\mathbf{x}}_{1\psi}$ is given by

$$
\hat{\mathbf{x}}_{1\psi} = \begin{pmatrix} \cos\psi\cos\eta \\ \cos\psi\sin\eta \\ -\sin\psi \end{pmatrix} \tag{A.6}
$$

The suffix ψ on δ and other differential variables indicates that the derivative is with respect to ψ.

The vector $\hat{\mathbf{R}}_1$ is a directional change perpendicular to the ray $\mathbf{R}_1$ (along $\hat{\mathbf{x}}_{1\psi}$) and is of length $d\psi$. This vector and $\hat{\mathbf{x}}_{1\psi}$ is a key building block for the others we want to derive.

The first vector we are interested in is $\mathbf{aA}_1$. From the Figure A.2, we see that it is the difference of two vectors as follows,

$$\begin{aligned} \mathbf{aA}_1 &= \mathbf{AA}_1 - \mathbf{Aa} \\ &= (\delta_\psi \mathbf{P_A}) - ((\delta_\psi \mathbf{P_A}) \cdot \hat{\mathbf{R}}_2)\hat{\mathbf{R}}_2 \end{aligned} \tag{A.7}$$

where $\delta_\psi \mathbf{P_A}$ is the vectorial shift in the point of intersection $\mathbf{P_A}$ of ray $\mathbf{R}_1$ and the first planar segment when the $\mathbf{R}_1$ is changed by angle $d\psi$. We have to derive $\hat{\mathbf{R}}_2$ and $\delta_\psi \mathbf{P_A}$ next to obtain $\mathbf{aA}_1$.

The unit-vector $\hat{\mathbf{R}}_2$ is the refracted ray, co-planar with $\hat{\mathbf{R}}_2$ and $\mathbf{n}_1$. It can be derived as a linear sum of vectors $\hat{\mathbf{R}}_2$ and $\mathbf{n}_1$. Following derivation of refracted ray in terms of incident ray and the normal, given in [29], we get,

$$\hat{\mathbf{R}}_2 = \frac{1}{n}\hat{\mathbf{R}}_1 + [\cos\theta_1 - \frac{\cos\theta}{n}]\mathbf{n}_1 \tag{A.8}$$

where n is the relative refractive index between the two media, θ is the angle of incidence ($\cos\theta = \mathbf{n}_1 \cdot \hat{\mathbf{R}}_1$) and θ_1 is the angle of refraction ($\cos\theta_1 = \mathbf{n}_1 \cdot \hat{\mathbf{R}}_2$). The two angles are related by Snells Law, $\sin\theta = n\sin\theta_1$

We derive the $\delta_\psi \mathbf{P_A}$ as follows. The point $\mathbf{P_A}$ is given by

$$\mathbf{P_A} = \hat{\mathbf{R}}_1 t_1 \tag{A.9}$$

where $t_1 = L_1$ is the scale along $\mathbf{R}_1$.

Hence, $\delta_\psi \mathbf{P_A}$ is given by,

$$\begin{aligned} \delta_\psi \mathbf{P_A} &= \hat{\mathbf{R}}_1 dt_1 + t_1(\delta_\psi \hat{\mathbf{R}}_1) \\ &= \hat{\mathbf{R}}_1 dt_1 + L_1(d\psi)\hat{\mathbf{x}}_{1\psi} \end{aligned} \tag{A.10}$$

To find t_1 we intersect the ray and the plane (with unit-normal $\mathbf{n}_1$). Any point $\mathbf{X}$ on the plane satisfies the relation,

$$\mathbf{n_1} \cdot \mathbf{X} + D_1 = 0 \qquad (A.11)$$

where D_1 is the distance of the plane from the origin.

Then putting $\mathbf{X} = t_1 \mathbf{\hat{R}_1}$, we would get,

$$t_1 = -\frac{D_1}{\mathbf{n_1} \cdot \mathbf{\hat{R}_1}} \qquad (A.12)$$

$$
\begin{aligned}
dt_1 &= \frac{D_1 (\mathbf{n_1} \cdot (\delta_\psi \mathbf{\hat{R}_1}))}{(\mathbf{n_1} \cdot \mathbf{\hat{R}_1})^2} \\
&= -\frac{t_1 (\mathbf{n_1} \cdot (\delta_\psi \mathbf{\hat{R}_1}))}{(\mathbf{n_1} \cdot \mathbf{\hat{R}_1})} \\
&= -\frac{L_1 (d\psi)(\mathbf{n_1} \cdot \mathbf{\hat{x}_{1\psi}})}{(\mathbf{n_1} \cdot \mathbf{\hat{R}_1})} \qquad (A.13)
\end{aligned}
$$

(where the last but one step is obtained from the previous Equation A.12 for t_1). We note that this dt_1 expression can be intuitively obtained geometrically as well.

We can put this last Equation A.13 in Equation A.10 and get,

$$\delta_\psi \mathbf{P_A} = L_1 d\psi [\mathbf{\hat{x}_{1\psi}} - \frac{(\mathbf{n_1} \cdot \mathbf{\hat{x}_{1\psi}})}{(\mathbf{n_1} \cdot \mathbf{\hat{R}_1})} \mathbf{\hat{R}_1}] \qquad (A.14)$$

Hence we can arrive at the expression for the required vector $\mathbf{aA_1}$ in terms of known quantities, and $d\psi$ by putting $\delta_\psi \mathbf{P_A}$ in Equation A.7.

$$
\begin{aligned}
\mathbf{aA_1} = \; & L_1 d\psi [\mathbf{\hat{x}_{1\psi}} - \frac{(\mathbf{n_1} \cdot \mathbf{\hat{x}_{1\psi}})}{(\mathbf{n_1} \cdot \mathbf{\hat{R}_1})} \mathbf{\hat{R}_1} \\
& - ((\mathbf{\hat{x}_{1\psi}} \cdot \mathbf{\hat{R}_2}) - \frac{(\mathbf{n_1} \cdot \mathbf{\hat{x}_{1\psi}})(\mathbf{\hat{R}_1} \cdot \mathbf{\hat{R}_2})}{(\mathbf{n_1} \cdot \mathbf{\hat{R}_1})}) \mathbf{\hat{R}_2}] \quad (A.15)
\end{aligned}
$$

where $\mathbf{\hat{R}_i}$ are the ray-vectors, $\mathbf{\hat{x}_{1\psi}}$ is the direction perpendicular to $\mathbf{\hat{R}_1}$, given in Equation A.6. $\mathbf{n_1}$ is the normal to the first interface, and the length L_1 is the intercept of ray $\mathbf{\hat{R}_1}$ at the first medium.

The other vector of interest is $\mathbf{DS_1}$. From the reference Figure we see

$$
\begin{aligned}
\mathbf{DS_1} &= \mathbf{Ds_1} + \mathbf{s_1 S_1} \\
&= \mathbf{cC_1} + L_3(\delta_\psi \hat{\mathbf{R}}_3) \quad\quad\quad\quad\quad\text{(A.16)}
\end{aligned}
$$

where we make use of the fact that $\mathbf{Ds_1} = \mathbf{cC_1}$ (by construction, in Figure A.2). The ray $\mathbf{C_1 s_1}$ is parallel to $\mathbf{R_3}$ and, therefore the vector $\mathbf{s_1 S_1}$ is the increment vector, $L_3(\delta_\psi \hat{\mathbf{R}}_3)$. $\delta_\psi \hat{\mathbf{R}}_3$ is the change in direction of the unit-vector ray $\hat{\mathbf{R}}_3$. Multiplication by the length L_3 is needed to get the arc-length swept by the ray.

This Equation shows that we have derive the vector $\mathbf{cC_1}$ (which can be derived in similar way as was done for $\mathbf{aA_1}$) and $(\delta_\psi \hat{\mathbf{R}}_3)$. We tackle $\mathbf{cC_1}$ first.

The vector $\mathbf{cC_1}$ is given by,

$$
\begin{aligned}
\mathbf{cC_1} &= \mathbf{CC_1} - \mathbf{Cc} \quad\quad\quad\quad\quad\quad\quad\quad\text{(A.17)} \\
&= \delta_\psi \mathbf{P_C} - (\hat{\mathbf{R}}_3 \cdot \delta_\psi \mathbf{P_C})\hat{\mathbf{R}}_3 \quad\quad\text{(A.18)}
\end{aligned}
$$

First we derive vector $\mathbf{CC_1}$ as the differential of the point of intersection of $\mathbf{R_2}$ and the second interface. The point $\mathbf{P_C}$ is given vectorially by,

$$
\mathbf{P_C} = \mathbf{P_A} + \hat{\mathbf{R}}_2 t_2 \quad\quad\quad\quad\quad\quad\text{(A.19)}
$$

where $t_2 = L_2$ denotes the scale.

Differentiating this, as we did before for $\mathbf{P_A}$, we get

$$
\begin{aligned}
\delta_\psi \mathbf{P_C} &= \delta_\psi \mathbf{P_A} + t_2(\delta_\psi \hat{\mathbf{R}}_2) + \hat{\mathbf{R}}_2 dt_2 \\
&= \delta_\psi \mathbf{P_A} + (L_2)(\delta_\psi \hat{\mathbf{R}}_2) + \hat{\mathbf{R}}_2 dt_2 \\
&= \delta_\psi \mathbf{P_A} + L_2(d\psi)\hat{\mathbf{x}}_{2\psi} + \hat{\mathbf{R}}_2 dt_2 \quad\quad\text{(A.20)}
\end{aligned}
$$

We know the first term from Equation A.14. The second two terms needs derivation of $\delta_\psi \hat{\mathbf{R}}_2$ and dt_2.

Taking the derivative of Equation A.8, we get $\delta_\psi \hat{\mathbf{R}}_2$ as

$$
\delta_\psi \hat{\mathbf{R}}_2 = [\frac{d\psi}{n}\hat{\mathbf{x}}_{1\psi} + (\delta_\psi F)\mathbf{n_1}] \qu\quad\quad\quad\text{(A.21)}
$$

64

where $F = \cos\theta_1 - \cos\theta/n$

$$
\begin{aligned}
\delta_\psi F & = \frac{\partial F}{\partial \psi} d\psi \\
& = d\psi\left(-\sin\theta_1 \frac{d\theta_1}{d\psi} + \frac{\sin\theta}{n}\frac{d\theta}{d\psi}\right) \qquad (A.22)
\end{aligned}
$$

To find $d\theta/d\psi$, we remember that $\cos\theta = \mathbf{n_1} \cdot \hat{\mathbf{R}}_1$.

Hence we get, $\sin\theta \frac{d\theta}{d\psi} = -\mathbf{n_1} \cdot \hat{\mathbf{x}}_{1\psi}$.

We can differentiate the Snell's Law, to get the relation between $d\theta$ and $d\theta_1$.

Thus we get, $\frac{d\theta_1}{d\psi} = \frac{d\theta}{d\psi}\frac{\cos\theta}{n\cos\theta_1}$

Substituting this in Equation A.22 after a little manipulation, we would get,

$$
\delta_\psi F \quad = \quad -\frac{d\psi}{n}\left(1 - \frac{\tan\theta_1}{\tan\theta}\right)(\mathbf{n_1} \cdot \hat{\mathbf{x}}_{1\psi}) \qquad (A.23)
$$

Putting Equation A.23 in

$$
\begin{aligned}
\delta_\psi \hat{\mathbf{R}}_2 & = \frac{d\psi}{n}\left[\hat{\mathbf{x}}_{1\psi} - \mathbf{n_1}\left(1 - \frac{\tan\theta_1}{\tan\theta}\right)(\mathbf{n_1} \cdot \hat{\mathbf{x}}_{1\psi})\right] \qquad (A.24) \\
& = (d\psi)\hat{\mathbf{x}}_{2\psi} \qquad (A.25)
\end{aligned}
$$

where (as was done for $\delta_\psi\hat{\mathbf{R}}_1$), in the last step, we define a vector corresponding to $\delta_\psi\hat{\mathbf{R}}_2$, given by

$$
\hat{\mathbf{x}}_{2\psi} = \frac{1}{n}\left[\hat{\mathbf{x}}_{1\psi} - \mathbf{n_1}\left(1 - \frac{\tan\theta_1}{\tan\theta}\right)(\mathbf{n_1} \cdot \hat{\mathbf{x}}_{1\psi})\right] \qquad (A.26)
$$

These vectors $\hat{\mathbf{x}}_{1\psi}$, $\hat{\mathbf{x}}_{2\psi}$ etc, have a **recursive** relationship (as evident from Equation A.26) which will help in generalizing the proof, as shown later.

To derive the last term dt_2 in Equation A.20 we have to find t_2 as the point of intersection of the ray $\mathbf{R_2}$ and the second interface (normal $\mathbf{n_2}$) and distance D_2. As a similar derivation was shown earlier, the details are left out.

$$t_2 = -\frac{(\mathbf{n_2} \cdot \mathbf{P_A}) + D_2}{(\mathbf{n_2} \cdot \hat{\mathbf{R}}_2)} \tag{A.27}$$

Taking the derivative and after some manipulations, we get

$$
\begin{aligned}
dt_2 &= -\frac{(\mathbf{n_2} \cdot \delta_\psi \mathbf{P_A})}{(\mathbf{n_2} \cdot \hat{\mathbf{R}}_2)} - \frac{t_2(\mathbf{n_2} \cdot \delta_\psi \hat{\mathbf{R}}_2)}{(\mathbf{n_2} \cdot \hat{\mathbf{R}}_2)} \\
&= -\frac{(\mathbf{n_2} \cdot \delta_\psi \mathbf{P_A})}{(\mathbf{n_2} \cdot \hat{\mathbf{R}}_2)} - \frac{L_2(d\psi)(\mathbf{n_2} \cdot \hat{\mathbf{x}}_{2\psi})}{(\mathbf{n_2} \cdot \hat{\mathbf{R}}_2)}
\end{aligned}
\tag{A.28}
$$

We note that this dt_2 expression can be intuitively obtained geometrically as well.

Substituiting Equation A.28 in Equation A.20 and rearranging we get,

$$
\begin{aligned}
\delta_\psi \mathbf{P_C} &= \delta_\psi \mathbf{P_A} - \hat{\mathbf{R}}_2 \Big[\frac{(\mathbf{n_2} \cdot \delta_\psi \mathbf{P_A})}{(\mathbf{n_2} \cdot \hat{\mathbf{R}}_2)}\Big] \\
&\quad + L_2(d\psi)\hat{\mathbf{x}}_{2\psi} - L_2(d\psi)\hat{\mathbf{R}}_2 \Big[\frac{(\mathbf{n_2} \cdot \hat{\mathbf{x}}_{2\psi})}{(\mathbf{n_2} \cdot \hat{\mathbf{R}}_2)}\Big]
\end{aligned}
\tag{A.29}
$$

This equation shows an useful **recursive** relation ($\delta_\psi \mathbf{P_C}$ in terms of $\delta_\psi \mathbf{P_A}$) to be used later.

We could get the full final form of $\delta_\psi \mathbf{P_C}$ (in terms of $d\psi$) by substituting $\delta_\psi \mathbf{P_A}$ from Equation A.14 into the above equation and rearranging,

$$\delta_\psi \mathbf{P_C} = (d\psi)[L_1(\hat{\mathbf{x}}_{\mathbf{1}\psi} - \frac{(\mathbf{n_1} \cdot \hat{\mathbf{x}}_{\mathbf{1}\psi})}{(\mathbf{n_1} \cdot \hat{\mathbf{R}}_\mathbf{1})}\hat{\mathbf{R}}_\mathbf{1})$$

$$-L_1\hat{\mathbf{R}}_\mathbf{2}(\frac{(\mathbf{n_2} \cdot \hat{\mathbf{x}}_{\mathbf{1}\psi})(\mathbf{n_1} \cdot \hat{\mathbf{R}}_\mathbf{1}) - (\mathbf{n_1} \cdot \hat{\mathbf{x}}_{\mathbf{1}\psi})(\mathbf{n_2} \cdot \hat{\mathbf{R}}_\mathbf{1}))}{(\mathbf{n_1} \cdot \hat{\mathbf{R}}_\mathbf{1})(\mathbf{n_2} \cdot \hat{\mathbf{R}}_\mathbf{2})})$$

$$+L_2\hat{\mathbf{x}}_{\mathbf{2}\psi} - L_2\hat{\mathbf{R}}_\mathbf{2}\frac{(\mathbf{n_2} \cdot \hat{\mathbf{x}}_{\mathbf{2}\psi})}{(\mathbf{n_2} \cdot \hat{\mathbf{R}}_\mathbf{2})}] \qquad (A.30)$$

We had set out to derive Equation A.18. We have almost got it except for an expression for $\hat{\mathbf{R}}_\mathbf{3}$. We write the latter now. From the standard formula for the refracted ray [29], we get,

$$\hat{\mathbf{R}}_\mathbf{3} = \frac{1}{n'}\hat{\mathbf{R}}_\mathbf{2} + [\cos \theta_t{}' - \frac{\cos \theta_t}{n'}]\mathbf{n_2} \qquad (A.31)$$

where $n' = \frac{C_2}{C_3}$ is the relative refractive index between Medium 2 and Medium 3, θ_t is the angle of incidence and $\theta_t{}'$ is the angle of refraction. The two angles are related by Snell's Law, $\sin \theta_t = n' \sin \theta_t{}'$

Hence substituting Equation A.31 and A.30 in Equation A.18 we would get the vector $\mathbf{cC_1}$.

The original goal was to derive $\mathbf{DS_1}$ as given in Equation A.16, expanded here in Equation A.32 for convenience.

$$\begin{aligned}\mathbf{DS_1} &= \mathbf{Ds_1} + \mathbf{s_1S_1} \\ &= \mathbf{cC_1} + L_3(\delta_\psi\hat{\mathbf{R}}_\mathbf{3}) \\ &= \delta_\psi\mathbf{P_C} - (\hat{\mathbf{R}}_\mathbf{3} \cdot \delta_\psi\mathbf{P_C})\hat{\mathbf{R}}_\mathbf{3} + L_3(\delta_\psi\hat{\mathbf{R}}_\mathbf{3}) \qquad (A.32)\end{aligned}$$

We derived $\delta_\psi\mathbf{P_C}$ so far. But we see that we need another factor, the differential change in the vector $\hat{\mathbf{R}}_\mathbf{3}$. We can derive this in the same identical way as done before for $\hat{\mathbf{R}}_\mathbf{2}$ and get,

67

$$\delta_\psi \hat{\mathbf{R}}_3 = \frac{d\psi}{n'}[\hat{\mathbf{x}}_{2\psi} - \mathbf{n}_2(1 - \frac{\tan\theta_t^{'}}{\tan\theta_t})(\mathbf{n}_2 \cdot \hat{\mathbf{x}}_{2\psi})] \quad (A.33)$$

$$= (d\psi)\hat{\mathbf{x}}_{3\psi} \quad (A.34)$$

where (as was done for $\delta_\psi \hat{\mathbf{R}}_1$ and $\delta_\psi \hat{\mathbf{R}}_2$), in the last step, we define a vector corresponding to $\delta_\psi \hat{\mathbf{R}}_3$, given by

$$\hat{\mathbf{x}}_{3\psi} = \frac{1}{n'}[\hat{\mathbf{x}}_{2\psi} - \mathbf{n}_2(1 - \frac{\tan\theta_t^{'}}{\tan\theta_t})(\mathbf{n}_2 \cdot \hat{\mathbf{x}}_{2\psi})] \quad (A.35)$$

We can therefore substitute Equations A.34 and A.30 in Equation A.32 to arrive at the vector $\mathbf{DS}_1$.

A.2   Differential vectors in dη-direction for three media

The analysis for the dη-direction is similar to last section, except we take the differentials with respect to dη and not dψ. The figure in the main text illustrating the flux-tube Figure A.1 is referred to when necessary instead of drawing a separate diagram showing the dη-ray exclusively. We write the final results here without detailed analysis, except when it is necessary to explain and illustrate a point of difference, specially when deriving the vector $\mathbf{DS}_2$.

The vector $\mathbf{R}_1$ is given in Equation A.3, reproduced here again for convenience.

$$\mathbf{R}_1 = L_1\hat{\mathbf{R}}_1 \quad (A.36)$$

$$= L_1 \begin{pmatrix} \sin\psi\cos\eta \\ \sin\psi\sin\eta \\ \cos\psi \end{pmatrix} \quad (A.37)$$

$$(A.38)$$

The "hat" over the vectors denotes unit-vectors as before.

The change in direction of $\mathbf{R_1}$ is given by,

$$
\begin{aligned}
\delta_\eta \hat{\mathbf{R}}_\mathbf{1} &= \frac{\partial \hat{\mathbf{R}}_\mathbf{1}}{\partial \eta} d\eta \\
&= d\eta \begin{pmatrix} -\sin\psi\sin\eta \\ \sin\psi\cos\eta \\ 0 \end{pmatrix} \qquad\qquad\text{(A.39)} \\
&= (d\eta)\hat{\mathbf{x}}_\mathbf{1\eta} \qquad\qquad\qquad\qquad\text{(A.40)}
\end{aligned}
$$

where the unit-vector $\hat{\mathbf{x}}_\mathbf{1\eta}$ is given by

$$
\hat{\mathbf{x}}_\mathbf{1\psi} = \begin{pmatrix} -\sin\psi\sin\eta \\ \sin\psi\cos\eta \\ 0 \end{pmatrix} \qquad\qquad\text{(A.41)}
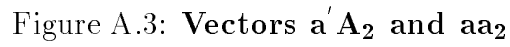$$

The suffix η on δ and other differential variables indicates that the derivative is with respect to η.

The change in the point of intersection (of $\mathbf{R_1}$ and first interface) $\mathbf{P_A}$, is given by

$$
\delta_\eta \mathbf{P_A} = L_1 d\eta [\hat{\mathbf{x}}_\mathbf{1\eta} - \frac{(\mathbf{n_1} \cdot \hat{\mathbf{x}}_\mathbf{1\eta})}{(\mathbf{n_1} \cdot \hat{\mathbf{R}}_\mathbf{1})}\hat{\mathbf{R}}_\mathbf{1}] \qquad\qquad\text{(A.42)}
$$

The vector $\mathbf{aa_2}$ (refer to Figure A.3) is almost identical in length and direction to $\mathbf{a^{'}A_2}$ (drawn perpendicular to ray $\mathbf{R_2}$ from point $\mathbf{A_2}$). The difference between these two vectors, $\mathbf{aa_2}$ and $\mathbf{a^{'}A_2}$ is of second order of length (arc swept by a differential length in going through a differential angle).

Hence we can derive the vector $\mathbf{aa_2}$ as

Figure A.3: **Vectors $\mathbf{a}'\mathbf{A_2}$ and $\mathbf{aa_2}$**

$$
\begin{aligned}
\mathbf{aa_2} &= \mathbf{a}'\mathbf{A_2} \\
&= \mathbf{AA_2} - \mathbf{Aa}' \\
&= (\delta_\eta \mathbf{P_A}) - ((\delta_\eta \mathbf{P_A}) \cdot \hat{\mathbf{R}}_2)\hat{\mathbf{R}}_2 \\
&= L_1 d\eta [\hat{\mathbf{x}}_{1\eta} - \frac{(\mathbf{n_1} \cdot \hat{\mathbf{x}}_{1\eta})}{(\mathbf{n_1} \cdot \hat{\mathbf{R}}_1)}\hat{\mathbf{R}}_1 \\
&\qquad - ((\hat{\mathbf{x}}_{1\eta} \cdot \hat{\mathbf{R}}_2) - \frac{(\mathbf{n_1} \cdot \hat{\mathbf{x}}_{1\eta})(\hat{\mathbf{R}}_1 \cdot \hat{\mathbf{R}}_2)}{(\mathbf{n_1} \cdot \hat{\mathbf{R}}_1)})\hat{\mathbf{R}}_2] \quad (A.43)
\end{aligned}
$$

The $\hat{\mathbf{R}}_2$ is given in Equation A.8. Taking the derivative with respect to $d\eta$, we would get,

70

$$\delta_\eta \hat{\mathbf{R}}_{\mathbf{2}} \quad = \quad \frac{d\eta}{n}[\hat{\mathbf{x}}_{\mathbf{1}\eta} - \mathbf{n_1}(1 - \frac{\tan\theta_1}{\tan\theta})(\mathbf{n_1} \cdot \hat{\mathbf{x}}_{\mathbf{1}\eta})] \qquad (A.44)$$

$$= \quad (d\eta)\hat{\mathbf{x}}_{\mathbf{2}\eta} \qquad\qquad\qquad (A.45)$$

where (as was done for $\delta_\eta\hat{\mathbf{R}}_{\mathbf{1}}$), in the last step, we define a vector corresponding to $\delta_\eta\hat{\mathbf{R}}_{\mathbf{2}}$, given by

$$\hat{\mathbf{x}}_{\mathbf{2}\eta} = \frac{1}{n}[\hat{\mathbf{x}}_{\mathbf{1}\eta} - \mathbf{n_1}(1 - \frac{\tan\theta_1}{\tan\theta})(\mathbf{n_1} \cdot \hat{\mathbf{x}}_{\mathbf{1}\eta})] \qquad (A.46)$$

The next step involves derivation of the change in the point of intersection (of $\mathbf{R_2}$ and second interface) $\mathbf{P_C}$. This follows, similar to derivation of Equations A.29 and A.30. We would get, therefore,

$$\delta_\eta\mathbf{P_C} \quad = \quad \delta_\eta\mathbf{P_A} - \hat{\mathbf{R}}_{\mathbf{2}}[\frac{(\mathbf{n_2} \cdot \delta_\eta\mathbf{P_A})}{(\mathbf{n_2} \cdot \hat{\mathbf{R}}_{\mathbf{2}})}]$$

$$+ L_2(d\eta)\hat{\mathbf{x}}_{\mathbf{2}\eta} - L_2(d\eta)\hat{\mathbf{R}}_{\mathbf{2}}[\frac{(\mathbf{n_2} \cdot \hat{\mathbf{x}}_{\mathbf{2}\eta})}{(\mathbf{n_2} \cdot \hat{\mathbf{R}}_{\mathbf{2}})}] \qquad (A.47)$$

And by substituiting $\delta_\eta\mathbf{P_A}$ from Equation A.42 we would get,

$$\delta_\eta\mathbf{P_C} \quad = \quad (d\eta)[L_1(\hat{\mathbf{x}}_{\mathbf{1}\eta} - \frac{(\mathbf{n_1} \cdot \hat{\mathbf{x}}_{\mathbf{1}\eta})}{(\mathbf{n_1} \cdot \hat{\mathbf{R}}_{\mathbf{1}})}\hat{\mathbf{R}}_{\mathbf{1}})$$

$$- L_1\hat{\mathbf{R}}_{\mathbf{2}}(\frac{(\mathbf{n_2} \cdot \hat{\mathbf{x}}_{\mathbf{1}\eta})(\mathbf{n_1} \cdot \hat{\mathbf{R}}_{\mathbf{1}}) - (\mathbf{n_1} \cdot \hat{\mathbf{x}}_{\mathbf{1}\eta})(\mathbf{n_2} \cdot \hat{\mathbf{R}}_{\mathbf{1}}))}{(\mathbf{n_1} \cdot \hat{\mathbf{R}}_{\mathbf{1}})(\mathbf{n_2} \cdot \hat{\mathbf{R}}_{\mathbf{2}})})$$

$$+ L_2\hat{\mathbf{x}}_{\mathbf{2}\eta} - L_2\hat{\mathbf{R}}_{\mathbf{2}}\frac{(\mathbf{n_2} \cdot \hat{\mathbf{x}}_{\mathbf{2}\eta})}{(\mathbf{n_2} \cdot \hat{\mathbf{R}}_{\mathbf{2}})}] \qquad (A.48)$$

Next we attempt to derive the vector $\mathbf{DS_2}$ in Figure A.1.
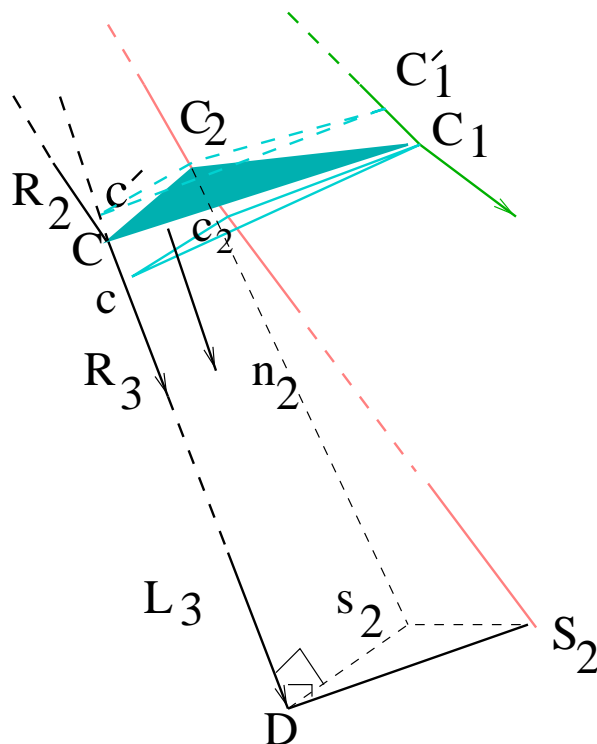
Figure A.4: **Construction of $\mathbf{DS_2}$**

Parts of Figure A.1 are redrawn in Figure A.4 for clarity and further construction. In Figure A.4 $\Delta \mathbf{cc_2 C_1}$ is the triangle formed by the points where the three-rays intersect the plane orthogonal to $\mathbf{R_3}$ passing through $\mathbf{C_1}$. In the main text, we show that ignoring second order differentials, this is a projection onto that orthogonal plane, passing through the point $\mathbf{C_1}$. In Figure A.4, we similarly get the triangle at $\mathbf{C_2}$, orthogonal to the ray $\mathbf{R_3}$, (extended backwards in dotted lines), meeting the other two rays at $\mathbf{c}'$, and $\mathbf{C_1}'$, respectively. This is also a projection, if we ignore second-order differentials. Hence, the two triangles $\Delta \mathbf{cc_2 C_1}$ and $\Delta \mathbf{c}' \mathbf{C_2 C_1}'$ (shown in dotted lines) are congruent (to first order of differentials).

To get the vector $\mathbf{DS_2}$ we concentrate on the dotted triangle, $\Delta \mathbf{c}' \mathbf{C_2 C_1}'$ in Figure A.4.

$$\mathbf{DS_2} = \mathbf{Ds_2} + \mathbf{s_2S_2}$$
$$= \mathbf{c}'\mathbf{C_2} + L_3(\delta_\eta\hat{\mathbf{R}}_3) \qquad \text{(A.49)}$$

$\mathbf{C_2S_2}$ is parallel to $\mathbf{R_3}$ and plane $\mathbf{Ds_2S_2}$ is orthogonal to $\mathbf{R_3}$ and $\delta_\eta\hat{\mathbf{R}}_3$ is the differential change in direction of $\hat{\mathbf{R}}_3$.

But, $\mathbf{c}'\mathbf{C_2}$ is given by,

$$\mathbf{c}'\mathbf{C_2} = \mathbf{CC_2} - \mathbf{Cc}' \qquad \text{(A.50)}$$
$$= \delta_\eta\mathbf{P_C} - (\hat{\mathbf{R}}_3 \cdot \delta_\eta\mathbf{P_C})\hat{\mathbf{R}}_3 \qquad \text{(A.51)}$$

We know $\delta_\eta\mathbf{P_C}$ from Equation A.48 and $\hat{\mathbf{R}}_3$ from Equation A.31. Substituting Equation A.51 in the Equation for $\mathbf{DS_2}$ we would get,

$$\mathbf{DS_2} = \delta_\eta\mathbf{P_C} - (\hat{\mathbf{R}}_3 \cdot \delta_\eta\mathbf{P_C})\hat{\mathbf{R}}_3 + L_3(\delta_\eta\hat{\mathbf{R}}_3) \qquad \text{(A.52)}$$

We are yet to derive the last term, in Equation A.52, involving $\delta_\eta\hat{\mathbf{R}}_3$. We can proceed as in previous section and to get,

$$\delta_\eta\hat{\mathbf{R}}_3 = \frac{d\eta}{n'}[\hat{\mathbf{x}}_{2\eta} - \mathbf{n_2}(1 - \frac{\tan\theta_t'}{\tan\theta_t})(\mathbf{n_2} \cdot \hat{\mathbf{x}}_{2\eta})] \qquad \text{(A.53)}$$
$$= (d\eta)\hat{\mathbf{x}}_{3\eta} \qquad \text{(A.54)}$$

where (as was done for $\delta_\eta\hat{\mathbf{R}}_1$ and $\delta_\eta\hat{\mathbf{R}}_2$), in the last step, we define a vector corresponding to $\delta_\eta\hat{\mathbf{R}}_3$, given by

$$\hat{\mathbf{x}}_{3\eta} = \frac{1}{n'}[\hat{\mathbf{x}}_{2\eta} - \mathbf{n_2}(1 - \frac{\tan\theta_t'}{\tan\theta_t})(\mathbf{n_2} \cdot \hat{\mathbf{x}}_{2\eta})] \qquad \text{(A.55)}$$

We can therefore substitute Equation A.48 and A.31 and Equations A.54 in Equation A.52 to arrive at the vector $\mathbf{DS_2}$.

A.3 Generalization to multiple media

The last two sections shows an underlying recursive pattern. We can derive a vector in the i-the layer in terms of vectors related to the $i - 1$-th layer. In this section we explicitly write the recursive relations. The details of the analysis are the same as last two sections and hence left out. The differentials are with respect to a general angle ν.
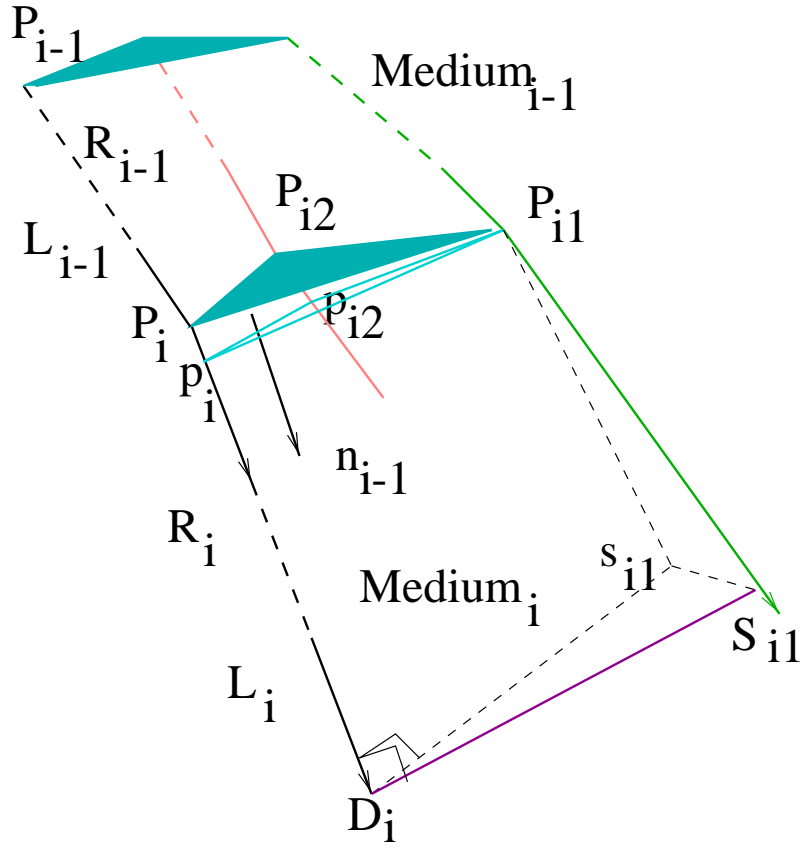

Figure A.5: **Rescursive Relations**

$$
\begin{aligned}
\mathbf{P_i} &= \mathbf{P_{i-1}} + \hat{\mathbf{R}}_{\mathbf{i-1}} t_{i-1} \\
&= \mathbf{P_{i-1}} + \hat{\mathbf{R}}_{\mathbf{i-1}} L_{i-1}
\end{aligned}
\tag{A.56}
$$

Taking the derivative, we get

$$
\begin{aligned}
\delta_\nu \mathbf{P_i} &= \delta_\nu \mathbf{P_{i-1}} + L_{i-1}(\delta_\nu \hat{\mathbf{R}}_{\mathbf{i-1}}) + \hat{\mathbf{R}}_{\mathbf{i-1}} dL_{i-1} \\
&= \delta_\nu \mathbf{P_{i-1}} + L_{i-1}(d\nu)\hat{\mathbf{x}}_{\mathbf{i-1}\nu} \\
&\quad - \hat{\mathbf{R}}_{\mathbf{i-1}}\left[\frac{(\mathbf{n_{i-1}} \cdot \delta_\nu \mathbf{P_{i-1}})}{(\mathbf{n_{i-1}} \cdot \hat{\mathbf{R}}_{\mathbf{i-1}})} + L_{i-1} d\nu \frac{(\mathbf{n_{i-1}} \cdot \hat{\mathbf{x}}_{\mathbf{i-1}\nu})}{(\mathbf{n_{i-1}} \cdot \hat{\mathbf{R}}_{\mathbf{i-1}})}\right] \\
&= \delta_\nu \mathbf{P_{i-1}} - \hat{\mathbf{R}}_{\mathbf{i-1}}\left[\frac{(\mathbf{n_{i-1}} \cdot \delta_\nu \mathbf{P_{i-1}})}{(\mathbf{n_{i-1}} \cdot \hat{\mathbf{R}}_{\mathbf{i-1}})}\right] \\
&\quad + L_{i-1}(d\nu)\hat{\mathbf{x}}_{\mathbf{i-1}\nu} - L_{i-1}(d\nu)\hat{\mathbf{R}}_{\mathbf{i-1}}\frac{(\mathbf{n_{i-1}} \cdot \hat{\mathbf{x}}_{\mathbf{i-1}\nu})}{(\mathbf{n_{i-1}} \cdot \hat{\mathbf{R}}_{\mathbf{i-1}})} \quad (A.57)
\end{aligned}
$$

Where the vector $\mathbf{x_i}$ is defined as follows and follows a recursive relation as well.

$$
\delta_\nu \hat{\mathbf{R}}_{\mathbf{i}} = (d\nu)\hat{\mathbf{x}}_{\mathbf{i}\nu} \tag{A.58}
$$

where $\hat{\mathbf{x}}_{\mathbf{i}\nu}$ is given by

$$
\hat{\mathbf{x}}_{\mathbf{i}\nu} = \frac{1}{n_{i-1}}[\hat{\mathbf{x}}_{\mathbf{i-1}\nu} - \mathbf{n_{i-1}}(1 - \frac{\tan\theta_{i-1}'}{\tan\theta_i})(\mathbf{n_{i-1}} \cdot \hat{\mathbf{x}}_{\mathbf{i-1}\nu})] \tag{A.59}
$$

The final length we want can be obtained in terms of all these vectors as,

$$
\mathbf{DS_{i1}} = \delta_\nu \mathbf{P_i} - (\hat{\mathbf{R}}_{\mathbf{i}} \cdot \delta_\nu \mathbf{P_i})\hat{\mathbf{R}}_{\mathbf{i}} + L_i(\delta_\nu \hat{\mathbf{R}}_{\mathbf{i}}) \tag{A.60}
$$